

**Particle-Laden Liquid Jet Impingement  
On A Moving Surface**

by

Hatef Rahmani

B.Sc., University of Tehran, 2013

A THESIS SUBMITTED IN PARTIAL FULFILLMENT OF

THE REQUIREMENTS FOR THE DEGREE OF

MASTER OF APPLIED SCIENCE

in

THE FACULTY OF GRADUATE AND POSTDOCTORAL STUDIES

(Mechanical Engineering)

The UNIVERSITY OF BRITISH COLUMBIA

(Vancouver)

May 2016

© Hatef Rahmani, 2016

## **Abstract**

In the railroad industry, coating of the rail with liquid changes the forces at the wheel-rail interface. Wet leaves on rail tracks can reduce the wheel-rail traction to dangerously low levels. To enhance wheel traction, railroads spray sand on the tracks. The sand may be applied in the form of a particle-laden jet.

The impingement of high-speed liquid jets on a moving surface was studied. The jet fluids were dilute suspensions of neutrally buoyant particles in water-glycerin solutions. At the low concentration studied, the suspension has a Newtonian fluid viscosity. A variety of jet and surface velocities, liquid properties, mean particle sizes, and volume fractions were studied. It was observed that for jets with very small particles, the addition of solids to the jet enhances deposition. In contrast, jets with larger particles in suspensions were more prone to splash than single phase jets of the same viscosity. It is speculated that the non-monotonic dependence of the splash threshold on the particle size occurs when the particle diameter is comparable to the lamella thickness.

Additionally, volume-of-fluid (VOF) CFD simulations were carried out to provide a full description of the flow field of a particle-free Newtonian jet spreading over a moving surface. The jet Reynolds number and Weber number of the simulations were in the range of 50-1000 and 100-8000, respectively. The simulations were generally in good agreement with experiments and they could successfully predict the lamella dimensions and velocity profiles.

## **Preface**

The authors of Chapter 2 are Hatef Rahmani and Dr. Sheldon Green. Dr. Green proposed the methodology to study the liquid jet impingement on low-speed and high-speed surfaces experimentally.

The authors of Chapter 3 are Hatef Rahmani and Dr. Sheldon Green. Dr. Green and representatives from L.B. Foster found the need to investigate the behavior of commercial Liquid Friction Modifier, namely ALLEVIATE®.

The authors of Chapter 4 are Hatef Rahmani and Dr. Sheldon Green. Dr. Green identified the need to experimentally study the Newtonian suspension jet impact on a moving surface. I studied and determined the variables and methodology with directions from Dr. Green. I wrote the manuscript with revisions from Dr. Green. A version of Chapter 3 will be submitted to a relevant journal in this field.

The authors of Chapter 5 are Hatef Rahmani and Dr. Sheldon Green. Dr. Green identified the need to simulate the liquid jet impingement on a moving surface. A version of this chapter has been accepted to appear in the CSME 2016 Conference Proceeding.

# Table of Contents

<b>Abstract.....</b>	<b>ii</b>
<b>Preface.....</b>	<b>iii</b>
<b>Table of Contents .....</b>	<b>iv</b>
<b>List of Tables .....</b>	<b>vii</b>
<b>List of Figures.....</b>	<b>viii</b>
<b>Glossary .....</b>	<b>xii</b>
<b>Acknowledgments .....</b>	<b>xiii</b>
<b>Chapter 1: Introduction .....</b>	<b>1</b>
1.1 Motivation .....	1
1.2 Liquid Friction Modifiers (LFMs) .....	2
1.3 Modes of Applications .....	2
1.4 Drop Impact on Stationary and Moving Surfaces.....	3
1.4.1 Particle-laden Drop Impact.....	5
1.5 Liquid Jet Impingement on Stationary and Moving Surfaces.....	6
1.5.1 Particle-laden Liquid Jet Impingement.....	8
1.6 Research Objectives .....	9
<b>Chapter 2: Methodology and Experimental Apparatus.....</b>	<b>11</b>
2.1 Air Cannon Set-up.....	11

2.1.1 High Speed Imaging in Air Cannon Set-up.....	13
2.1.2 Spray System .....	14
2.1.3 Air Cannon Electrical Control .....	15
2.2 Spinning Disk Set-up .....	16
2.2.1 High Speed Imaging in Spinning Disk Set-up.....	18
2.3 Test Liquids.....	18
2.3.1 Flow Rate Measurement.....	21
<b>Chapter 3: Commercial Liquid Friction Modifier (ALLEVIATE®) .....</b>	<b>22</b>
3.1 ALLEViate® Properties .....	22
3.2 Flow Rate Measurements .....	25
3.3 Impingement on Moving Surface.....	27
3.4 Wind Tunnel.....	31
<b>Chapter 4: Newtonian Suspension Jet Impingement .....</b>	<b>34</b>
4.1 Glass Bead Suspensions .....	38
4.2 Polyester Suspensions .....	45
4.3 A Model for Jet Impingement .....	52
<b>Chapter 5: Numerical Simulation of a Liquid Jet Impinging on a Moving Substrate.....</b>	<b>57</b>
5.1 Numerical Method.....	59
5.1.1 Governing Equations .....	59
5.1.2 Dimensionless Governing Equations.....	60

5.1.3 Meshing and Boundary Conditions .....	61
5.1.4 Mesh Independency Check.....	62
5.1.5 Validation With Experiment.....	64
5.2 Results and Discussions .....	66
<b>Chapter 6: Conclusions and Recommendations .....</b>	<b>70</b>
6.1 Conclusions for Liquid Friction Modifier (ALLEVIATE®).....	70
6.2 Conclusions for Newtonian Suspension Jets Impingement on a Moving Surface.....	71
6.3 Conclusions for Numerical Simulation of Laminar Liquid Jet Impingement.....	72
6.4 Recommendations for Future Work.....	72
<b>Bibliography .....</b>	<b>74</b>

## **List of Tables**

Table 2-1 Average roughness height for different steel plates .....	13
Table 2-2 Properties of liquid tests: pure water-glycerin and glass beads suspensions.....	20
Table 4-1- Fitted k and K for particle-laden jets impingement for various particle size, volume fraction, and surface roughness.....	56

## List of Figures

Figure 1-1 Two possible outcomes of steady state jet impingement: (a) deposition, (b) splash. The surface is moving from left to right. ....	7
Figure 2-1 Air cannon set-up .....	12
Figure 2-2 Wooden projectile with metal surface.....	13
Figure 2-3 High speed imaging set-up for air cannon apparatus .....	14
Figure 2-4 Control box for air cannon .....	16
Figure 2-5 Spinning disk set-up .....	17
Figure 2-6 Hall Effect sensor set-up .....	17
Figure 2-7 High speed imaging set-up for spinning disk apparatus .....	18
Figure 3-1 Particle size distribution of ALLEViate® .....	22
Figure 3-2 Shear stress versus shear rate .....	23
Figure 3-3 Viscosity versus shear rate .....	23
Figure 3-4 Viscosity at very low shear stress .....	24
Figure 3-5 ALLEViate® flow rate versus nozzle back pressure.....	25
Figure 3-6 Discharge coefficient for ALLEViate® as a function of Reynolds number .....	26
Figure 3-7 Splash-deposition map for ALLEViate® with different viscosities for the surface roughness of 0.152 $\mu\text{m}$ .....	28
Figure 3-8 Splash-deposition map for the surface roughness of 0.152 $\mu\text{m}$ : a) base liquid of ALLEViate®, b) ALLEViate®.....	29
Figure 3-9 High-speed images for ALLEViate® jet impingement: a) Deposition b) Splash ...	30
Figure 3-10 Lamella width variation with surface speed at constant jet velocity .....	31
Figure 3-11 Flow rate as a function of jet velocity for different wind speeds.....	32

Figure 3-12 Deflection of ALLEViate® steady jet for different jet velocities, wind speed is 19.9 m/s and flows from left to right. ....	33
Figure 4-1 Contact angle as a function of suspension volume fraction .....	35
Figure 4-2 Rheology test for glass beads suspension: (a) shear stress vs shear rate, (b) relative viscosity vs shear rate .....	37
Figure 4-3 Rheology test for polyester suspension: relative viscosity vs shear rate .....	38
Figure 4-4 Discharge coefficient as a function of Reynolds number .....	39
Figure 4-5 Time series of jet impact on a moving surface: a) particle-free liquid jet, b) particle-laden jet with volume fraction of 10%. The substrate is moving from left to right at 14.76 m/s. ....	40
Figure 4-6 Instability in particle-laden jet, red arrow a) particle-free liquid b) particle-laden flow .....	41
Figure 4-7 Splash-deposition map regime for 65% glycerin-35% water. Red lines show the threshold for particle-free jets and blue lines show the threshold for particle-laden jets. ....	42
Figure 4-8 Splash-deposition map regime for 85% glycerin-15% water. ....	42
Figure 4-9 Splash regime map for particle-laden jet at a constant surface speed of 14.76 m/s. Surface roughness is 0.15 $\mu\text{m}$ and the average particle size is 15 $\mu\text{m}$ .....	43
Figure 4-10 Splash regime map for particle-laden jet at a constant surface speed of 8.71 m/s. Surface roughness is 0.15 $\mu\text{m}$ and average particle size is 15 $\mu\text{m}$ .....	44
Figure 4-11 Error bands for splash thresholds (blue lines). Test conditions are given in the caption of Figure 4-10. ....	45
Figure 4-12 Jet instability for different jet velocities.....	46
Figure 4-13 Polyester suspension jet at nozzle exit .....	47

Figure 4-14 Splash-deposition map regime for 85% glycerin-15% water. Blue line shows the threshold for large particles in a jet.....	48
Figure 4-15- Splash-deposition map regime for 75% glycerin-25% water. Red lines show the threshold for particle-free jets and blue lines show the threshold for particle-laden jets. ....	49
Figure 4-16 Splashing regime map for particle-laden jet at a constant surface speed of 8.71 m/s. Surface roughness is 0.15 $\mu\text{m}$ and average particle size is 180 $\mu\text{m}$ .....	49
Figure 4-17 Splashing regime map for particle-laden jet at a constant surface speed of 8.71 m/s. Surface roughness is 0.3 $\mu\text{m}$ and average particle size is 180 $\mu\text{m}$ .....	51
Figure 4-18- Error bands for splash thresholds (blue lines). Test conditions are given in the caption of Figure 4-17. ..	51
Figure 4-19- Model proposed for drop impact and jet impingement.....	53
Figure 4-20 Comparison of experimental results with model predictions. Points are the data from experiments and threshold lines are fitted from jet impact modeling for given conditions. ....	55
Figure 5-1 Schematic of the computational domain used for the simulations with the associated boundary conditions (Top), typical computational mesh used in the simulation (bottom) .....	62
Figure 5-2 Free surface profile around the impingement point for the typical coarse mesh (top) and intermediate mesh (bottom). .....	63
Figure 5-3 Velocity profile within the lamella thickness for different mesh intensities. The conditions are given in the caption of Figure 3.....	64
Figure 5-4 Lamella dimensions (top view of jet impingement) .....	65
Figure 5-5 W/R versus surface speed for constant jet velocity of 12 m/s and viscosity of 65.3 $\text{mPa.s}$ .....	65
Figure 5-6 Path-line of liquid jet impinging on a moving surface.....	66

Figure 5-7 Outcome of jet impact for simulation and experiment, a) Deposition, b) Splash..... 67

Figure 5-8 R/D and W/D versus surface speed at constant jet velocity of 12m/s ..... 68

Figure 5-9 Horizontal velocity profiles within lamella..... 69

## Glossary

$D$	Jet diameter
$V_{jet}$	Jet velocity
$V_{surface}$	Surface speed
$\mu$	Viscosity
$\mu_e$	Effective viscosity
$\rho$	Density
$\sigma$	Surface tension
$\epsilon$	Surface roughness
$\varphi$	Particle volume fraction
$d_p$	Mean particle size
$\rho_p$	Particle density
$Re$	Reynolds number
$We$	Weber number
$Stk$	Stokes number
$R$	Lamella radius
$W$	Lamella width
$h$	Lamella thickness
$C_d$	Discharge coefficient

## **Acknowledgments**

First and foremost I would like to express my sincere gratitude to my graduate supervisor Prof. Sheldon Green for his never-ending support, patient guidance, and immense knowledge throughout the course of this research. His positive outlook and confidence in my research inspired me. Without his offering to accomplish this research, I would not be able to finish it.

I would like to thank Kelsan Technological Corporation and NSERC for support of this research. I would also like to extend my gratitude to engineers from LB Foster, Mr. John Cotter, Dr. Louisa Stanlake, Mr. Dave Elvidge, and Dr. Richard Stock for their continuous support and motivation.

For important discussions and critical review, I thank my colleagues Dr. Ali Vakil, Amir Farzad Foroughi, and Amirhossein Salimian, and also the members of my research group at the Applied Fluid Mechanics Laboratory, Yuchen Guo, Quinn Mulligan, Alireza Sarraf Shirazi, Morgan Hibbert, and Justin Robert.

Lastly, I want to thank my parents and beloved brother and sister for all the moral support and the amazing chances they've given me over the years. I thank them for giving me strength to reach for the stars and chase my dreams. I will remain eternally in their debt.

# **Chapter 1 : Introduction**

## **1.1 Motivation**

Rail transport is one the most energy efficient and cost-effective forms of freight and passenger transportation in North America. The Canadian railroad consists of more than 72,000 Kilometers of track, and transports more than 270 million tons of freight and 70 million people annually [1]. Railways will continue to increase their influence as alternative methods such as ground and air freight less cost effective. It has been demonstrated that through an integrated approach of effectively managing the railway transport, fuel consumption and wear on the rail can be significantly reduced [2, 3]. Thus, the railroad industry, including L.B foster, is conducting research to improve the efficiency of rail transportation.

Friction at the wheel-rail interface is understood to have significant impacts on both wheel and rail wear, lateral (curving) forces, curve noise, and fuel efficiency. Through applying a friction modifying agent on the wheel-rail interface, called top of rail (TOR) friction control, the railroad industry can reduce the fuel consumption by 6-9%, lateral forces on the rail track, and wheel-rail wear [2, 3]. Additionally, other studies have shown that this method leads to a reduction in noise, track corrugation, and damage from rolling contact fatigue, which is a major cause of derailment [4]. Although recent research has been conducted to discover the benefits of TOR, it is still considered a novel approach and is not yet fully utilized in the railroad industry.

## **1.2 Liquid Friction Modifiers (LFMs)**

Currently, research is devoted to the development of highly effective liquid friction modifier (LFM). They are usually made up of water-based suspended polymers and inorganic solids. Kelsan Technological Corporation has produced several liquid friction modifiers for various applications. One of the primary LFMs is a water-based suspension, named KELTRACK®, which is a non-Newtonian fluid with shear thinning and viscoelastic behavior. Field trials have shown that coating the rail surface with the LFM reduced fuel consumption, rail-wheel wear, and greenhouse gas emissions [1].

The applications of LFMs can occur in heavily deciduous forested areas, where wet leaves on rail tracks can reduce the wheel-rail traction to dangerously low levels. This phenomena is called Low Railhead Adhesion in which contamination of the railhead causes trains to experience less grip. This can lead to wheel-slip when the train is taking power, and wheel-slide when the train is braking. To overcome this condition, the railroad is coated with a high-friction material. The coating method usually involves spraying sand on to the rail. Therefore, LB Foster has developed another LFM specifically for mitigating this problem, called ALLEViate®. ALLEViate® is also a non-Newtonian suspension which includes large sand particles (0.2-0.4 mm) and has shear thinning and viscoplastic behavior.

## **1.3 Modes of Applications**

Liquid friction modifiers can be deposited onto the railhead through the use of a trackside applicator or through use of on-board spray systems (the focus in this research). The liquid friction

modifiers are applied to the top of rail through on-board spray systems, called air-blast atomizers. They are typically mounted underneath the locomotives and at least 76 mm above the rail surface, and transfer the liquid in the form of ligaments and droplets.

However, there are some inherent problems in this method which makes it less desirable. First of all, droplets and ligaments atomized through spray systems can be excessively deflected by a cross wind. Considering the presence of a cross wind and the non-uniformity of droplet size, air blast nozzles produce highly non-uniform coverage along the rail, resulting in poor transfer efficiency. Additionally, this form of LFM application is difficult to implement on many railroad locomotives because the required high volume, high pressure air supply may not be accessible.

An alternative option was proposed to apply LFMs to the railhead through a steady continuous liquid jet instead of atomization as any difficulties are eliminated. Liquid jets are less susceptible to crosswind effects owing to their lower drag-to-inertia ratio. The proposed spraying system is more simple and allows for perfect control over the rate of LFM application. Also, it does not need the high volume and high pressure air supply, which was previously required by atomizing nozzles.

## **1.4 Drop Impact on Stationary and Moving Surfaces**

The interaction of liquid droplets on stationary and moving surfaces has received much attention due to its applications in electrical, agricultural, automotive and gas turbine industries. Droplet impact behavior on a dry, solid surface is very complex and this phenomenon is still not entirely understood. Over the past century, many researchers studied the drop impaction experimentally and numerically. The outcome of drop impaction depends on the impact velocity, drop size, the properties of the liquid (density, viscosity, viscoelasticity, and other non-Newtonian

behaviors of rheological complex fluids), the surface or interfacial tension, the roughness and wettability of the solid surface, the non-isothermal effects (e.g., solidification and evaporation), and air entrapment [5-7].

Rioboo et al. [7] showed that the results of droplet impaction on stationary surfaces can be categorized into six categories: deposition, prompt splash, corona splash, receding breakup, partial rebound, and complete rebound. Range et al. [8] studied more specifically the effects of surface roughness on the impaction outcome and have concluded that surface roughness lowers the splash threshold significantly. Mundo et al. [9] used two rotating discs with different surface roughnesses ( $\varepsilon/D \sim 0$  or 1) and their results indicate that for a rough surface, the droplet size distributions vary only slightly with increasing K value and non-dimensional surface roughness determines the distribution of droplet size ( $K = We \cdot Oh^{0.4}$ ;  $We$  and  $Oh$  are impact Weber number and Ohnesorge number, respectively).

Chen et al. [10], Povarov et al. [11], and Courbin et al. [12] investigated the drop impaction on a moving surface and observed that the tangential speed plays a significant role on impaction outcome and, thus, included this variable in their splash-deposition threshold parameterization. Chen et al. [10] introduced the tangential velocity by impacting Newtonian droplets on a spinning disk. He reported that the tangential Weber number is of particular significance. The tangential component of velocity is obtained by combining the disk rotational speed and the angle of drop impact. Povarov et al. [11] accordingly studied the drop impaction on a moving surface and observed that the air boundary layer, caused by disk rotation, leads to drop detachment from surface.

Recently, Bird et al. [13] proposed a model for the outcome of drop impaction on a moving surface considering the lamella growth rate. His model is based on a balance between droplet

kinetic energy and surface energy. He showed that splash occurs once the drop kinetic energy is considerably greater than the surface energy. In his model, the kinetic energy of the lamella is  $\rho(V_l - V_t)^2 L^2 h$  and the surface energy scales as  $\gamma h L$ , where  $V_l$  is the lamella velocity, and  $V_t$  is the tangential component of velocity.

$$\frac{\rho(V_l - V_t)^2 L}{\gamma} > C \gg 1 \quad (1-1)$$

### 1.4.1 Particle-laden Drop Impact

More recently, owing to many industrial applications, attention has been given to the liquids containing particles [14, 15]. Several works have studied the suspension drops impaction on stationary substrates. Based on current models for suspension drop impaction, splash occurs when the value of  $K = We_d^{1/2} Re_d^{1/4}$  is greater than the critical value  $K_0$ , where  $We_d$  and  $Re_d$  are Weber and Reynolds numbers based on drop radius [16]. In these models, addition of particles only changes the value of viscosity from  $\mu$  to  $\mu_e$ , the effective viscosity. Effective viscosity is increasing with volume fraction. Thus, it is speculated that a suspension drop is less likely to splash than a liquid drop. However, Nicholas [15] observed that the addition of particles decreased the splash-deposition threshold. Subsequently, Peters et al. [17] and Grishaevev [18] reported the inapplicability of the concept of effective viscosity as it fails to consider volume fraction,  $\varphi$ , particle size,  $d_p$ , and particle density,  $\rho_p$ , simultaneously.

Peters et al. [17], instead, studied the dependence of splash onset on both  $d_p$  and  $\rho_p$ , and proposed a model for dense suspension droplets,  $\varphi = 0.62 \pm 0.03$ . By finding the ratio of drop kinetic energy to surface energy, they derived the model from an energy balance at particle level:

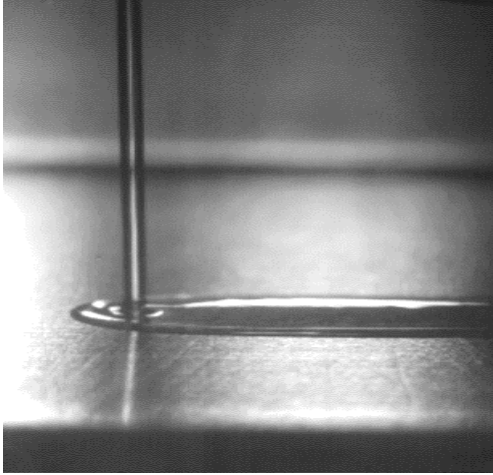
$$\frac{E_{kin}}{E_{surf}} \sim \frac{1}{6} \frac{\rho_p r_p U^2}{\sigma} = \frac{1}{6} We_p \quad (1 - 2)$$

Where  $We_p$  is a particle-based Weber number. Grishaev [18] deviated from these models and proposed the criterion for suspension drop impact using particle velocity, not drop velocity. He hypothesized that collisions between particles may lead to higher velocity for solid spheres in a liquid. He described that for larger particles, 200 and 370  $\mu m$ , splash is more likely to occur for higher volume fractions.

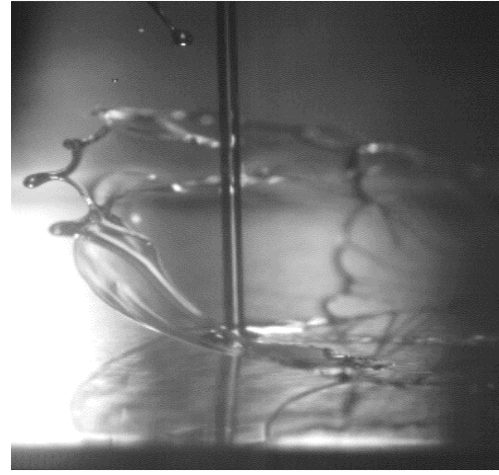
## 1.5 Liquid Jet Impingement on Stationary and Moving Surfaces

The impingement of high-speed Newtonian and non-Newtonian liquid jets on stationary and moving surfaces is relevant to a number of industrial processes, including impingement cooling and surface coating. Liquid jet impingement is salient to the railroad industry, where coating of the rail with Liquid Friction Modifier (LFM) changes the forces at the wheel-rail interface. There are only limited studies in literature investigating the liquid jet impingement on a moving substrate. The majority of studies are related to liquid jet impingement on stationary surface, aimed at understanding the hydraulic jump and heat transfer processes.

When a circular liquid jet impinges on the substrate, it forms an ultra-thin layer of fluid, called lamella. If the substrate is moving, the lamella is convected into a U-shape that is superficially similar to the Rankine Half Body of potential flow, although viscosity plays a key role in determining the lamella geometry (Figure 1-1(a)). Depending on the jet properties and the substrate speed (Keshavarz et al. [19]), the lamella may be lifted off the substrate producing the splash (Figure 1-1(b)).



(a)



(b)

Figure 1-1 Two possible outcomes of steady state jet impingement: (a) deposition, (b) splash. The surface is moving from left to right.

Watson [20] and Nakoryakov et al. [21] experimentally investigated free surface liquid jets on stationary substrate and developed a mathematical model. Zumbrunnen [22] showed that flow behavior and heat transfer efficiency is significantly affected when surface moves. Gradeck et al. [23] performed experimental and numerical studies of an axisymmetric water jet on a moving surface for different nozzle diameters (17 and 20 mm), jet and surface velocities. Fujimoto et al. [24] provided the description of flow fields of a circular water jet impinging on a pre-coated moving surface. In comparison with this study, these experiments were performed at very low jet and surface velocities.

For the high speed jet impact on a fast moving surface, Keshavarz et al. [19] reported that the key parameters are fluid viscosity, surface tension, jet velocity, surface speed, and surface roughness. He further developed a model for splash-deposition threshold for jet impingement based on an energy balance proposed initially by Bird et al. [13]. He also found that increasing the surface roughness reduces the splash threshold, leading to lower transfer efficiency.

Kumar [25] experimentally examined the effects of viscosity on a high speed liquid jet and reported a three-regime splashing-spreading pattern. Additionally, he proved that increasing both surface and jet velocities raises the splash probability. Recently, Moulson and Green [26] have shown that the air surrounding the lamella plays an essential role in lamella detachment. By reducing the air pressure below a threshold, lamella detachment and the following splash are completely suppressed.

Guo [27] studied the surface roughness impacts on outcome of liquid jet impingement on a fast moving surface. He visualized that while jet and surface speeds were both salient, splash was more likely to occur on surfaces with higher roughness. He also made detailed measurements of the dimensions of the liquid surface. Shirazi [28] focused on transient jet impingement on a moving substrate. For various jet and surface speeds, viscosity, and surface roughness, he reported the same trend for outcome of transient jet impact.

### **1.5.1 Particle-laden Liquid Jets Impingement**

Little is known in literature about particle-laden liquid jet impingement on stationary and moving surfaces, and it is considered as a relatively new and emerging field. Only Yamamura et al. [29] visualized that addition of solid spheres to jets assists the wetting productivity in coating process. He experimentally revealed that air entrainment into the liquid jet, impinging on a moving surface, is postponed if particles are added. They used spherical particles with diameter ranging from 8 to 30  $\mu m$ , which are comparable to the particles used in this study. They also dispersed the particles in Newtonian liquids.

## **1.6 Research Objectives**

Railroad transport is one of the most efficient methods for freight and passenger transportation in North America. Through applying Liquid Friction Modifiers to the Top-of-Rail surface, aimed at controlling friction and lateral forces, the railroad industry increases the transfer efficiency. When LFM<sub>s</sub> are applied from a moving train, not all of the product will adhere to the railroad tracks. The “transfer efficiency” is defined to be that portion of the dispensed product that adheres to the top of the rail.

One of the common LFM<sub>s</sub> (ALLEVIATE®), produced by Kelsan Technological Corporation, is utilized in slippery rail conditions. ALLEViate® contains large sand particles to enhance wheel-rail traction. Currently, the railroad industry uses air blast atomizers to spray LFM<sub>s</sub> to the railhead; however, due to the problems mentioned previously, attention has been given to steady circular liquid jet instead. Field trials have proved that the latter method is more efficient and easier to be implemented.

Although several researchers studied liquid jet impingement on a fast moving surface, little is known what happens if particles are added. Therefore, the objective of this research is to investigate the Newtonian and non-Newtonian suspension jets impingement for different variables: jet and surface speeds, viscosity, orifice diameter, particle size, and volume fraction. In this application it is important to understand how particulate-laden jets interact with a moving substrate. Additionally, the splash-deposition threshold will be quantified for each case.

To supplement experimental data for a pure liquid jet, CFD simulations are carried out to provide a full description of the flow field of a laminar Newtonian jet spreading over a smooth

moving surface. The jet Reynolds number and Weber number of the simulations are respectively in the range of 50-1000 and 100-8000. The jet-to-surface velocity ratio is in the range of 0.2-1.5. The simulations results are validated with experiments.

## **Chapter 2 : Methodology and Experimental Apparatus**

Two custom-fabricated devices, a low-speed (air cannon) and a high-speed (spinning disk), are used in this research. They are constructed specifically to allow for a wide range of surface speeds. Depending on the required surface speed, the suitable device is chosen.

### **2.1 Air Cannon Set-up**

For low to medium surface speeds (up to 25 m/s), a linear traverse system was used to provide the moving surface. The linear traverse, constructed by Dressler [30], is a pneumatic-energy-powered system designed to accelerate the projectile to the desired speed. The projectile is constructed from wood with a section of steel plate, representing the rail surface, mounted on the top.

Figure 2-1 shows the components of the linear traverse system. The air tank is connected to the air compressor and has the capacity to deliver up to 100 psi pressure. The projectile is first inserted into the end of the barrel. The spray nozzle, which is solenoid-actuated, is opened and liquid jet is emitted from nozzle. The solenoid poppet valve is then quickly opened and the tank, which was initially pressurized, releases compressed air immediately into the barrel. This rapid pressurization forces the projectile to move quickly along the barrel. At the barrel exit, the projectile passes underneath the nozzle and the impingement is recorded by high speed camera. At the end, there is a stopping mechanism to remove the kinetic energy of projectile. For safety considerations, this apparatus can provide a maximum speed of 25 m/s, which is equivalent to 60 psi tank pressure.

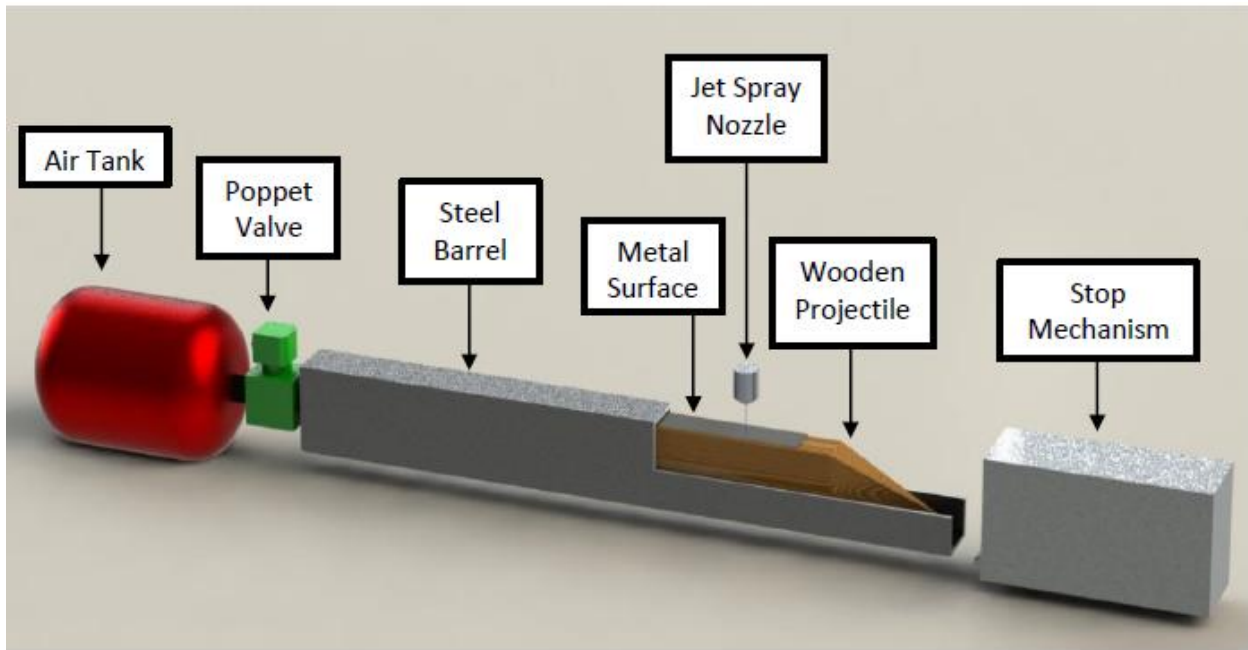


Figure 2-1 Air cannon set-up

This set-up is designed to approximate a real railroad. The frame of reference has been changed for easier implementation. The wooden projectile (Figure 2-2) is used as a light-weight carrier for the impingement surface which is a stainless steel plate. The projectile has a 13 mm thick and 76.2 mm wide polished steel surface. The dimension of the projectile is close to that of the barrel to minimize the air leakage and optimize the projectile shooting. A 1/8" thick rubber sheet was mounted on the back of the projectile to make sure that the projectile is moving tight inside the barrel. The leading part of the projectile was shaped into a nose which made it aerodynamically efficient and also a barb was added underneath so that the projectile is secured appropriately.



Figure 2-2 Wooden projectile with metal surface

Three different grades of sand papers were used to study the effect of surface roughness on impact. The roughness of the surface was measured by a commercial profilometer. Roughness was measured at different locations and in different directions. The average values for various plates are presented in Table 2-1.

Table 2-1 Average roughness height for different steel plates

Surface		Average height ( $\mu m$ )
Type	ID	
Mirror	#8	0.019
Smooth	P400	0.152
Rough	P60	0.302

### 2.1.1 High Speed Imaging in Air Cannon Set-up

Vision Research Phantom v611 high-speed cine camera was used to visualize the steady pure liquid and particle-laden liquid jets on a moving surface. This camera uses a fast wide screen

CMOS sensor to for high frame rates and high resolutions. Several Navitar lenses were used in these sets of experiments, particularly the Navitar Zoom 7000 lens. Most of the images were taken at 20,000 frames per second with a 380x320 resolution. A 1 KW high-intensity light source was used to illuminate the impact point. A light diffuser plate, as demonstrated in figure below, was placed between light source and wooden projectile for more clear visualization and filming. Figure 2-3 shows the high speed imaging set-up designed specifically for this linear traverse system.

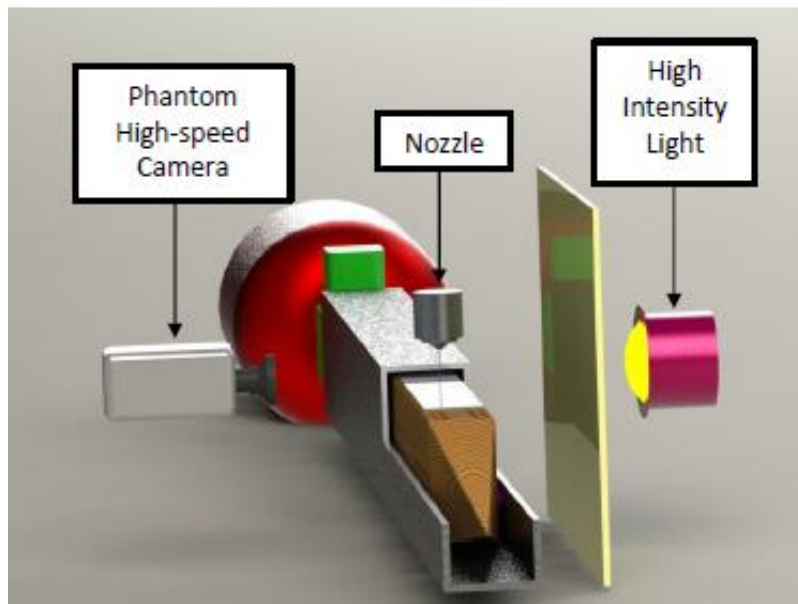


Figure 2-3 High speed imaging set-up for air cannon apparatus

### 2.1.2 Spray System

Three nozzles were used in this research with 0.8, 1.30, and 1.71 mm diameter orifices. Large orifice size is chosen to make sure that large particles do not clog the nozzle. The nozzle is mounted 7.6 cm from the disk surface, which is a good representation of the real distance between the sprayer and the rail track. To generate the steady liquid jet, an accumulator was employed. The accumulator was first filled with the test liquid and then pressurized by nitrogen gas. Depending

on the nozzle size and liquid properties, the accumulator was able to produce a steady jet with a velocity up to 30 m/s. A pressure transducer, installed immediately upstream of the nozzle, recorded the nozzle back pressure. A solenoid valve controlled the flow. One advantage of this setup was its ability to provide more stable nozzle back pressures than pumps.

### **2.1.3 Air Cannon Electrical Control**

A control box is designed to allow for precise control over components during impingement. In this set-up, it is really important to open the solenoid valve and turn on/off the light and other components at the right time and sequence. At maximum surface speed, jet impingement on moving substrate lasts only for 10 milliseconds, and images should be taken during that period. Although this kind of high-speed camera has the ability to capture around 900 milliseconds of video, it is not feasible to trigger it manually. Thus, an electrical control system is essential for proper operation. The control system consists of a National Instrument Data Acquisition 6009 and an optical sensor, which is placed at the barrel exit. When the projectile passes by this optical sensor, the movement is detected, the valve is opened, the light source is turned on, and the camera is triggered.



Figure 2-4 Control box for air cannon

## 2.2 Spinning Disk Set-up

The spinning disk is shown schematically in Figure 2-5. The spinning disk apparatus, which was constructed specifically for these experiments, allows for precise control over surface speed, jet velocity and surface roughness. The liquid jet emitted by the nozzle impinges on a moving disk. The disk radius is about 30 cm and this device has the ability to provide surface speed from 10 m/s (500 rpm) to 100 m/s (3000 rpm). The disk is driven by a variable frequency drive (VFD) motor. Half of the disk circumference was roughened and other half was not to study the effects of surface roughness on jet impact outcome more easily. Again, the commercial profilometer was used to measure the roughness heights in vertical and horizontal directions.

A similar spray system was employed to generate the steady jet. The only difference is, as shown in Figure 2-7, a solenoid-actuated flow interrupter was installed downstream of the nozzle

tip to remove the transient associated with jet start-up. Once the jet had stabilized, normally after 2 seconds, the flow interrupter was de-activated and a stable jet impinged on the moving substrate.

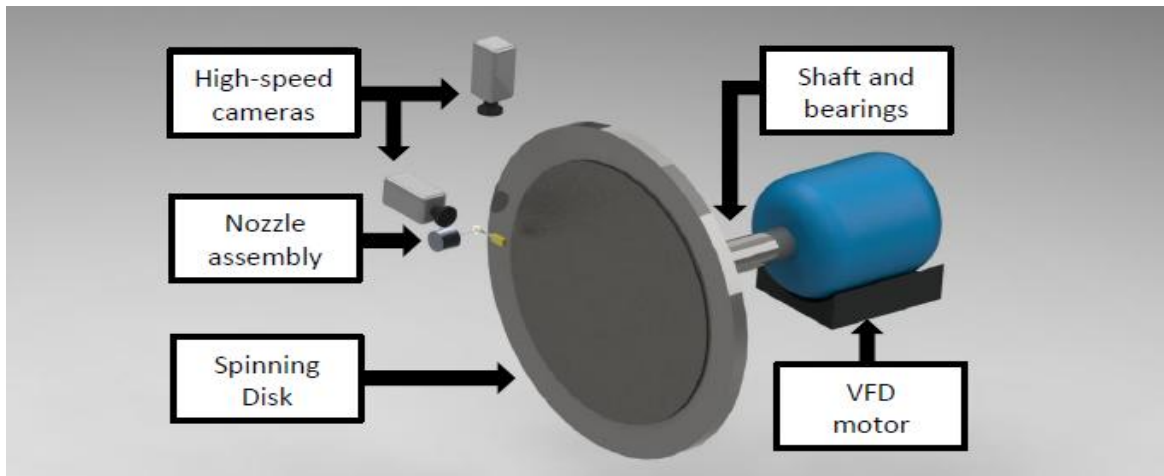


Figure 2-5 Spinning disk set-up

Several researchers reported that the surface roughness has a critical role in determining the outcome of jet impingement. Roughness height is not uniform throughout the surface. Thus, for higher repeatability, jet should impinge on the same location each time. A Hall Effect sensor was installed in front of the disk surface. Every time the sensor sees the magnet, it actuates the nozzle and impingement occurs immediately.



Figure 2-6 Hall Effect sensor set-up

## 2.2.1 High Speed Imaging in Spinning Disk Set-up

The liquid jet impingement onto the substrate was visualized using two high speed cameras (a Phantom V611 high-speed camera and a Phantom V7 high-speed camera) from two different angles at the same time, as depicted in Figure 2-7. The images were recorded at 20,000 frames per second and 380x320 resolution. From the captured high-speed images it was possible to determine the lamella attachment or detachment for a particular condition. Two high intensity light sources, fiber optic (MO150, JH Technologies) and 6700 Lumen white LED array with collimating lens, were employed to illuminate the fields-of-view of the cameras.

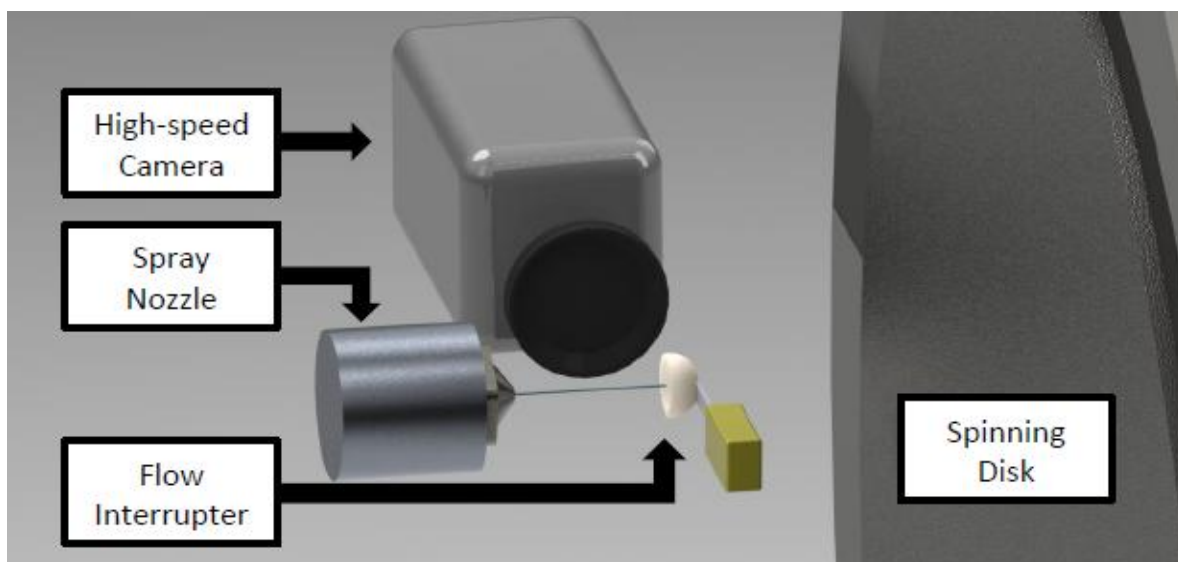


Figure 2-7 High speed imaging set-up for spinning disk apparatus

## 2.3 Test Liquids

Chapter 3 of this research includes the results for ALLEViate®, commercial liquid friction modifier which was produced by Kelsan Technological Corporation recently. ALLEViate® consists of 250  $\mu\text{m}$  sand particles for improving wheel-rail traction in slippery rail conditions.

Kelsan provides this suspension for lab experiments, thus there is no sample preparation required. However, rheological properties of ALLEVIATE® will be discussed in length in this chapter.

Chapter 4 fundamentally studies the physics of adding particles to Newtonian jets. Different mixtures of water-glycerin solutions were used as the base liquids. By changing the glycerin percentage, it was possible to cover a wide range of viscosity from 18.1 to 76.9 mPa.s. Impingement tests were done for these liquids with various combinations of jet and surface velocities.

Two separate particles were dispersed in Newtonian liquids and studied experimentally: 1. Hollow glass spheres with a mean size of  $15 \mu\text{m}$ , standard deviations from their mean size of 8% to 12%, and density of  $(1.1 \pm 0.05) \times 10^3 \frac{\text{kg}}{\text{m}^3}$ , 2. Polyester particles with a mean size of  $180 \mu\text{m}$ , standard deviations from their mean size of 15% to 25%, and density of  $(1.15 \pm 0.08) \times 10^3 \frac{\text{kg}}{\text{m}^3}$ . The particles density was matched to the density of base fluid to produce a neutrally buoyant suspension. Depending on the volume fractions, the flow may remain in Newtonian regime or turn into the non-Newtonian suspension [31]. Thus, the solids concentrations were chosen to be very small, typically up to 10%, to ensure that the dilute suspension is still Newtonian when it impinges the surface.

To ensure the uniform water-glycerin solution as well as homogeneous suspension, samples were continuously mixed 24 hours before usage. Subsequently, suspensions were placed into a Bench-Top Ultrasonic Bath to remove entrained air bubbles. The Ultrasonic bath also helps to separate the clustered particles and guarantees a uniform particle-laden flow. Small amounts of surfactant were added to the sample during the sonication to prevent agglomeration on the surface.

Measurements showed that this small amount does not change the rheological behavior of suspensions.

The rheological data was measured using HAAKE VT550 viscometer with shear rate operating up to  $1000\text{ s}^{-1}$ . For the low concentrations, the suspension shows Newtonian behavior, but for very high volume fraction, i.e. 32%, the suspension starts showing shear thinning behavior. Only viscosity increases when particles are present. To match the viscosity, the glycerin percentage for the suspension base liquid was chosen slightly smaller, as presented in Table 2-2, to allow for this viscosity increase. The exact value was determined by fitting the theoretical model to the experiment data and re-measuring the viscosity. Surface tension was measured by du Noüy ring apparatus for both particle-free and particle-laden liquids. The results, Table 2-2, suggest that particles only make extremely slight changes in the values of surface tension, and that cannot be responsible for any change in outcome of jet impact.

Table 2-2 Properties of liquid tests: pure water-glycerin and glass beads suspensions

Liquid (glycerin %)	Glass beads volume fraction (%)	Density [ $\text{kg}\cdot\text{m}^{-3}$ ]	Viscosity [ $\text{mPa}\cdot\text{s}$ ]	Surface Tension [ $\text{mN}\cdot\text{m}^{-1}$ ]
70	0	1175.8	18.14	66.4
68.4	5	1174.1	18.06	66.2
66.1	10	1173.6	18.10	66.1
75	0	1185.32	28.72	66.1
73.2	5	1182.8	28.23	66
71.5	10	1182.1	29.15	65.8
80	0	1192.3	47.83	65.6
77.9	5	1188.8	46.78	65.3
76.2	10	1187.4	47.41	65.2
85	0	1209.4	76.92	65.2
83.3	5	1205.8	76.3	65.0
82.5	10	1204.7	77.1	64.9

### **2.3.1 Flow Rate Measurement**

Initially, experiments on the spray system were conducted with the test liquids at different nozzle back pressures to gain essential information of the following liquid jet properties: jet diameter, jet speed and volumetric flow rate. Due to the difficulties associated with accurately measuring the liquid volume, mass flow rates were recorded instead and then used in the calculation of volumetric flow rate.

To measure the mass flow rate, the liquid flowed through the nozzle via the activation of an upstream solenoid valve for a duration of two seconds. During this period of time, the resultant liquid jet was deflected by a flow-interrupter to remove any potential transient effects. Then, the flow-interrupter, which is solenoid-actuated, was de-activated quickly to let the liquid jet flow freely into a beaker for collection. For each measurement, the jet flow was permitted for a duration of 30 seconds. The weight of the sprayed liquid was measured on a precision balance. Combining that with an average nozzle back pressure recorded during the 30-second jet flow, a graph could be plotted for each liquid/nozzle combination to show mass flow rate characteristics. From the mass continuity equation, the jet average velocity could be calculated.

# Chapter 3 : Commercial Liquid Friction Modifier (ALLEVIATE®)

## 3.1 ALLEVIATE® Properties

ALLEVIATE® is a liquid friction modifier LB Foster uses for slippery rail condition. It is a water-based suspension including relatively large sand particles for better rail traction. The particles volume fraction is about 28%. Preliminary studies to quantify particle sizes were achieved and are presented in Figure 3-1.

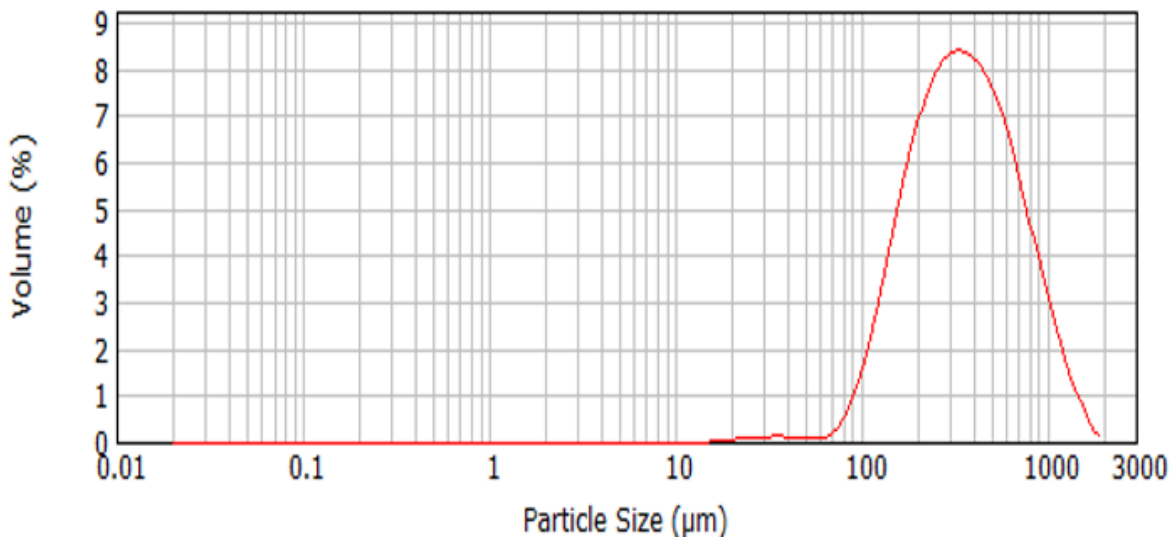


Figure 3-1 Particle size distribution of ALLEVIATE®

The average size of particles is between 0.2 and 0.4 mm. Nozzle orifice size is chosen to be five times greater than the average particle size to avoid the nozzle clogging. Considering that the maximum particle is about 2 mm, orifice diameter was then chosen to be 2.1 mm. Rheological data was measured with HAAKE VT550 viscometer. The shear rate varied from 0 to 120  $s^{-1}$  (Figures 3-2 and 3-4).

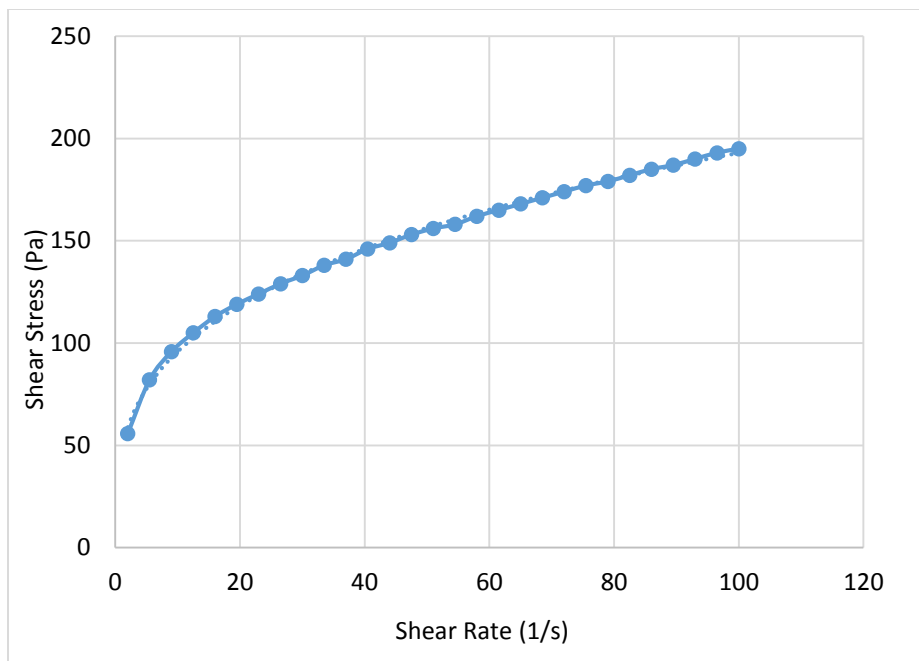


Figure 3-2 Shear stress versus shear rate

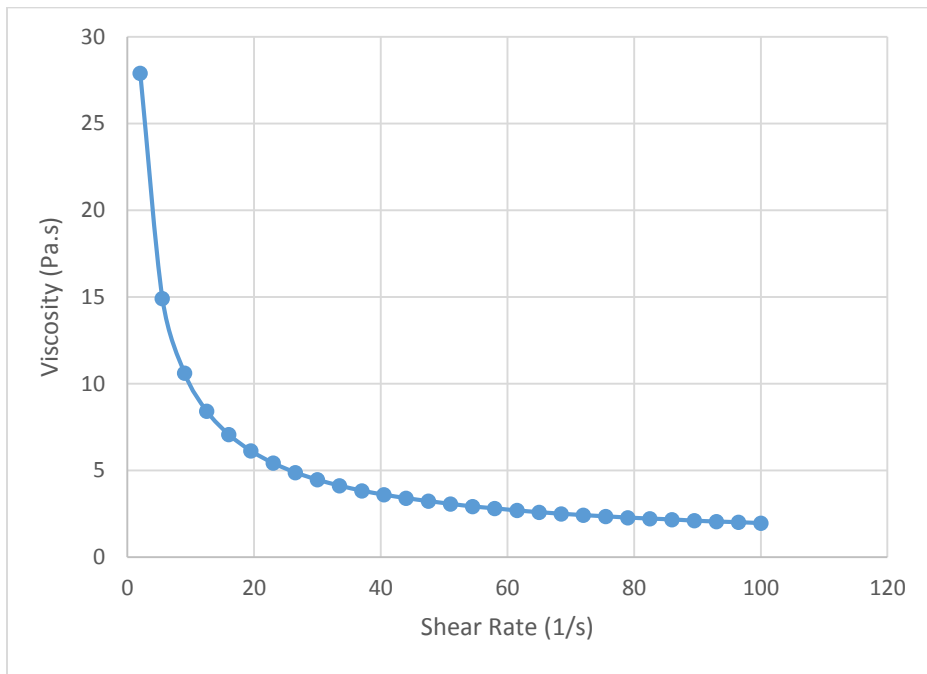


Figure 3-3 Viscosity versus shear rate

The viscosity decreased while the applied shear rate was increased, indicating that ALLEViate® is a non-Newtonian fluid with shear thinning behavior. Similarly, the yield stress of the fluid was investigated to completely describe the rheological behavior. Viscosity is plotted for low shear rates in Figure 3-4. The curve peak is at  $0.12\text{ s}^{-1}$  shear rate, which associates to a 10.8 Pa yield stress.

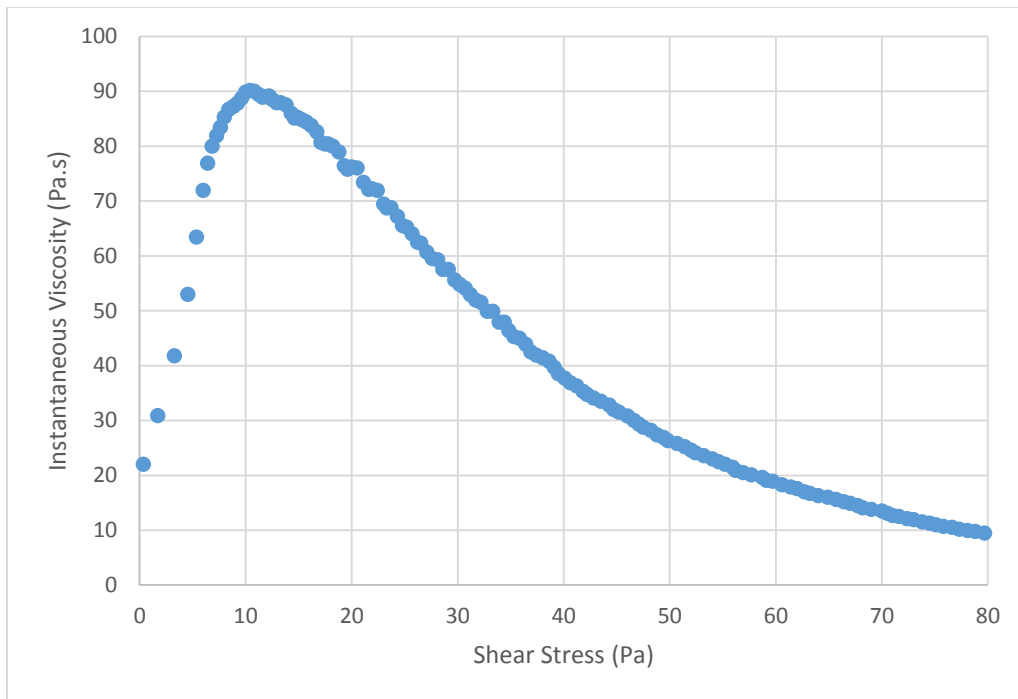


Figure 3-4 Viscosity at very low shear stress

The general form of shear stress for non-Newtonian flows are:

$$\tau = \tau_y + k\dot{\gamma}^n \quad (3 - 1)$$

Where  $\tau_y$ ,  $k$ , and  $n$  are yield stress, consistency coefficient, and power law index, respectively.

The model was fitted to the rheological data and the fitting parameters were adjusted to be  $k = 47.06$  and  $n = 0.303$  to give reasonable agreement. It is worth mentioning that the value of  $n$  for shear thinning fluids should be smaller than one.

### 3.2 Flow Rate Measurements

Figure 3-5 shows the volumetric flow rate of ALLEViate® as a function of nozzle back pressure. To isolate the viscous effects, three solutions with varying viscosities were used. ALLEViate® viscosity at  $100\text{ s}^{-1}$  is 1.4 Pa.s. Two other samples were prepared with viscosities of 0.7 and 3.5 Pa.s, namely low viscosity and high viscosity ALLEViate®. All other properties, including particle size and volume fraction, were kept constant. Solutions of higher viscosity show lower flow rate due to higher viscous losses at the orifice.

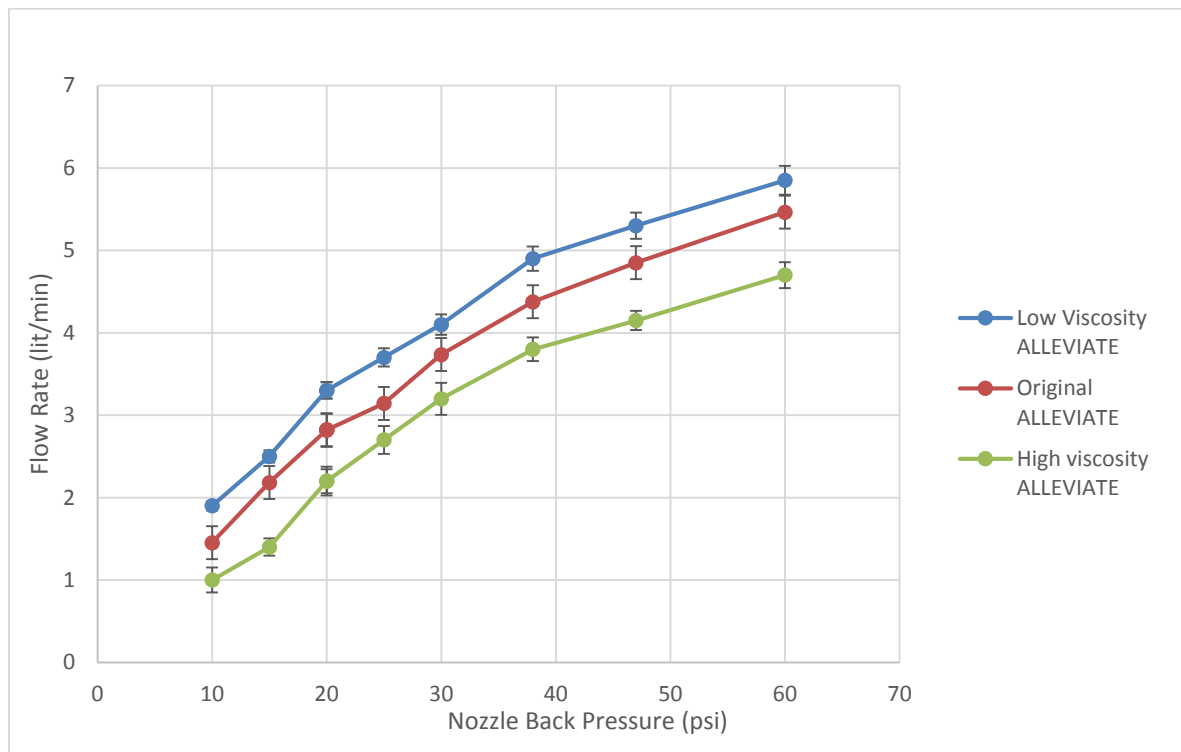


Figure 3-5 ALLEViate® flow rate versus nozzle back pressure

Mass flow rate also provides useful information about the fluid flow losses as it passes through the nozzle. For the Newtonian fluids, only two parameters are required to characterize

these losses at the nozzle discharge: Discharge Coefficient ( $c_d$ ) and Reynolds Number ( $Re$ ). This coefficient is defined as

$$C_d = \frac{\text{Experimental mass flow rate } (\dot{m})}{\text{Theoretical mass flow rate}} = \frac{\dot{m}}{A_j(\sqrt{2\Delta P \rho})} \quad (3 - 2)$$

The theoretical mass flow rate can be obtained from the Bernoulli's equation. Since the ALLEVIADE® viscosity is not constant, the viscosity at a certain shear rate is considered for the Reynolds number calculation. This shear rate is based on jet velocity and diameter and is as follows

$$Re = \frac{\rho V_{jet} D}{K \left( \frac{V_{jet}}{2D} \right)^{n-1}} \quad (3 - 3)$$

Figure 3-6 shows the discharge coefficient for ALLEVIADE®. Discharge coefficient is increasing proportionally with Reynolds numbers, and at large Reynolds number it goes to 0.8.

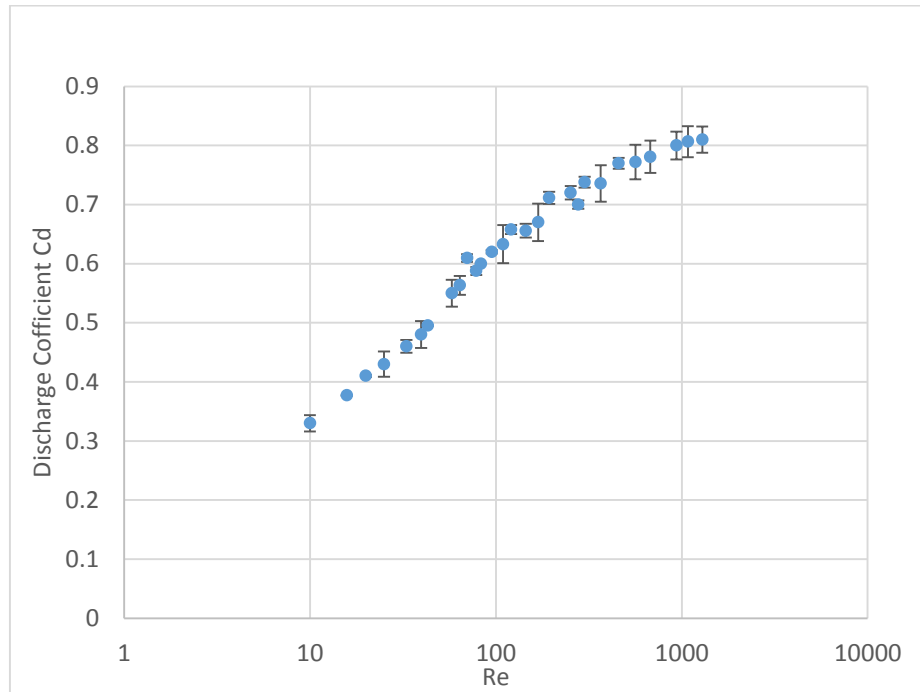
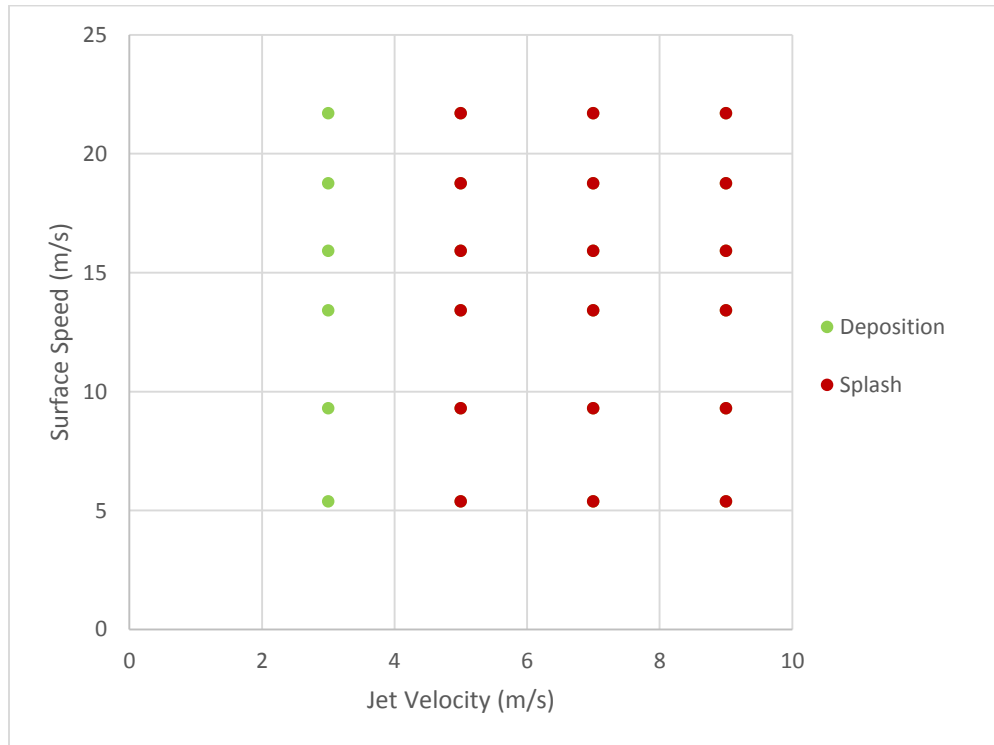


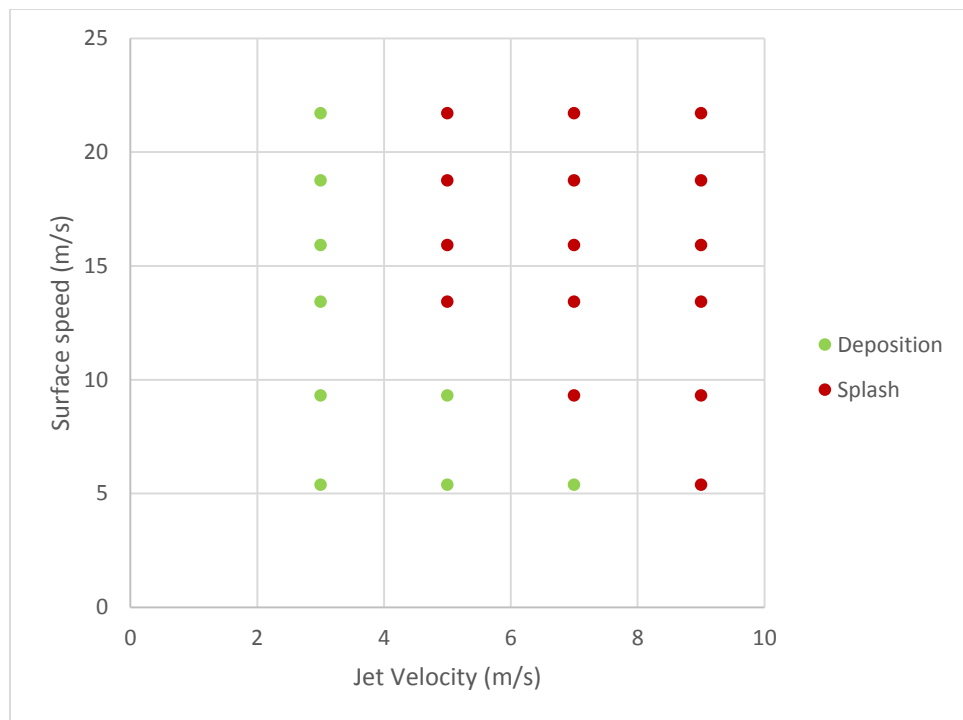
Figure 3-6 Discharge coefficient for ALLEVIADE® as a function of Reynolds number

### 3.3 Impingement on Moving Surface

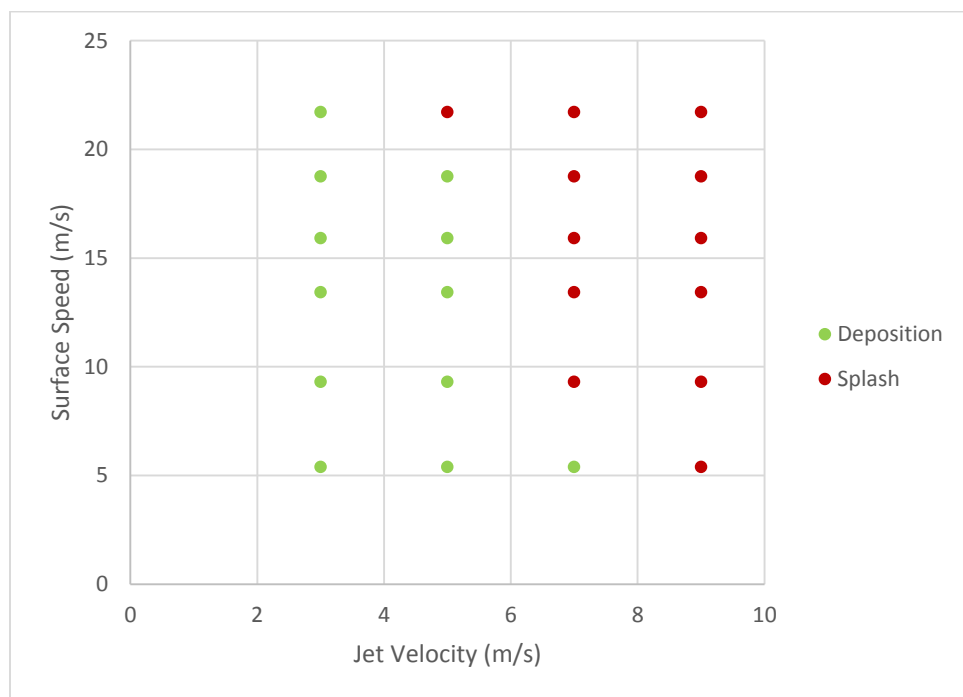
The ALLEViate® was impinged onto a moving surface in a form of steady jet. A low speed air cannon apparatus was used for this set of experiments. Jet and surface velocities were varied between 4-13 m/s and 5-25 m/s, respectively. The 2.1 mm nozzle was used for these tests. The tests were conducted on smooth steel surface ( $0.152 \mu\text{m}$  roughness height). In these graphs, each scatter points represents one experiment. Green points show deposition, which is our desired case, and red points show splash.



(a)



(b)



(c)

Figure 3-7 Splash-deposition map for ALLEViate® with different viscosities for the surface roughness of 0.152  $\mu\text{m}$ : a) low viscosity ALLEViate®, b) Original ALLEViate®, c) high viscosity ALLEViate®

As observed, for a given jet and surface velocities, splash is more likely to occur for solutions with a lower viscosity. This is consistent with previous finding for particle-free liquid jet (Keshavarz et al. [19] and Kumar [25]). The same experiments were carried out but on rough surface ( $0.302 \mu\text{m}$ ). The general trend again agrees well with previous reports, i.e. larger surface roughness enhances splash. However, the dependence of splash threshold on roughness height is lower for particle-laden jet than a pure liquid.

To investigate the physics of particle addition to liquid jet, splash-deposition map for both particulate and particle-free liquids are plotted in Figure 3-8. Figure 3-8(a) shows the deposition regime for ALLEViate® base fluid and Figure 3-8(b) shows the same graph when sand particles are present. The particle addition has modest impacts on splash threshold as it only changes three points from deposition to splash. Thus, the low transfer efficiency of ALLEViate® is mainly caused by the properties of base fluid, not particle addition. This topic will be discussed in length in chapter 4, where particles are added to a Newtonian steady jet.

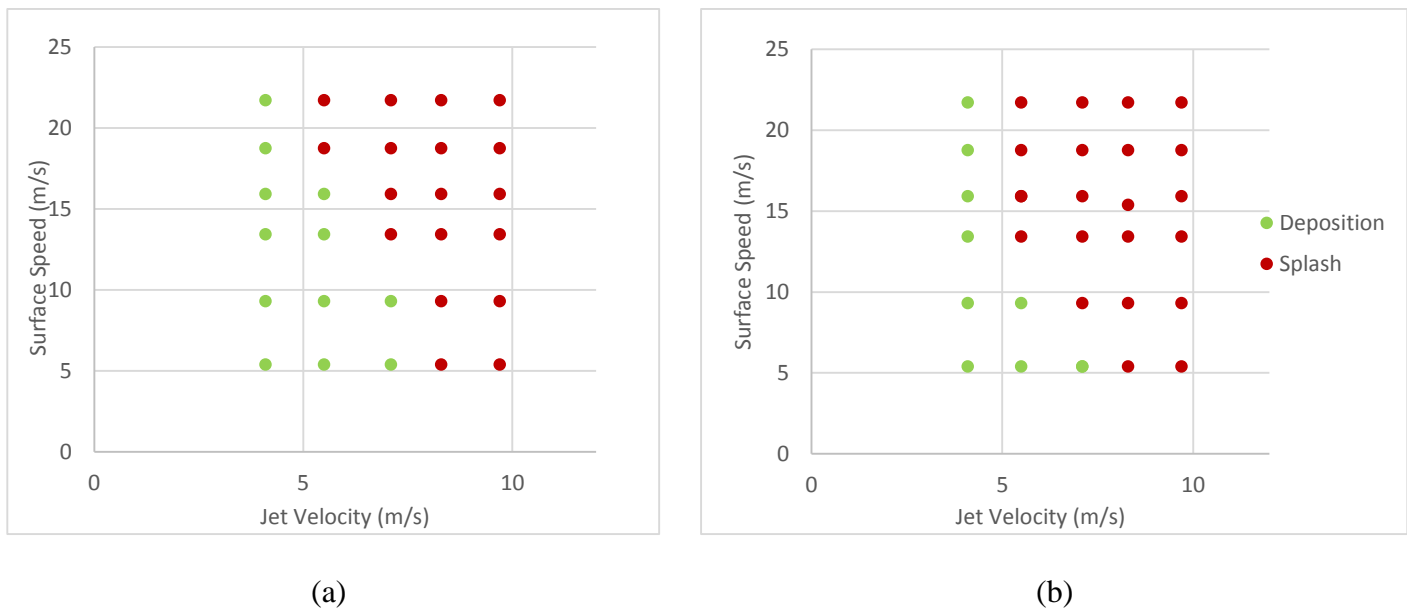


Figure 3-8 Splash-deposition map for the surface roughness of  $0.152 \mu\text{m}$ : a) base liquid of ALLEViate®, b) ALLEViate®

Figure 3-9 shows two possible outcomes of ALLEViate® jet impingement on moving surface. The images were recorded with high-speed camera at 20,000 frame per second. They both are for surface speed of 5.2 m/s but for different jet velocities. The left figure displays deposition while right one displays splash.

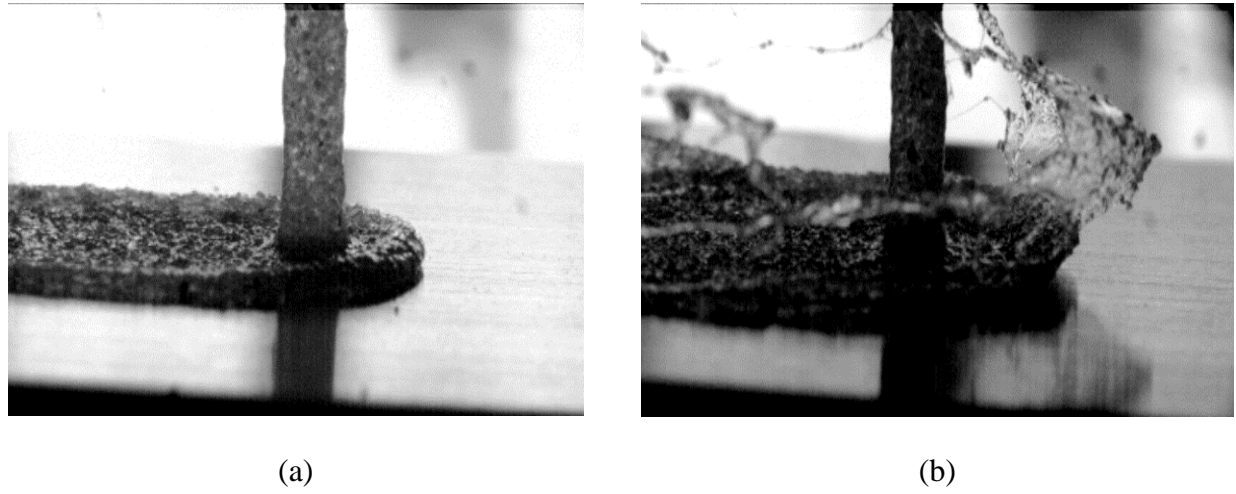
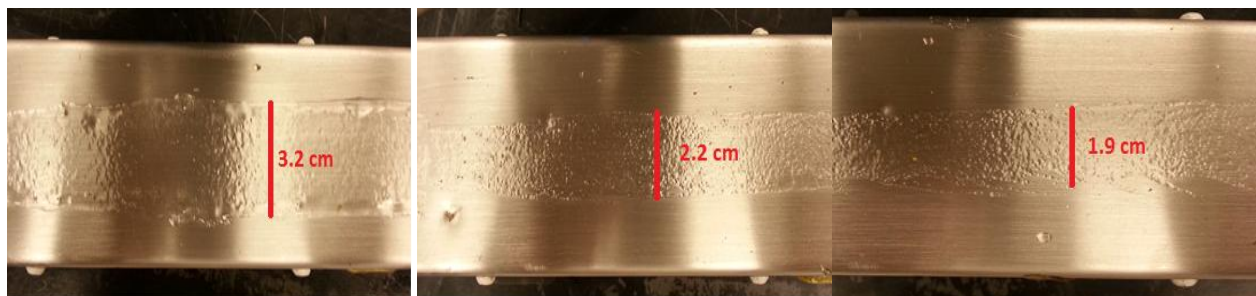


Figure 3-9 High-speed images for ALLEViate® jet impingement: a) Deposition ( $V_{jet} = 4.2 \frac{m}{s}$  and  $V_{surface} = 5.2 \frac{m}{s}$ ), b) Splash ( $V_{jet} = 9.7 \frac{m}{s}$  and  $V_{surface} = 5.2 \frac{m}{s}$ )

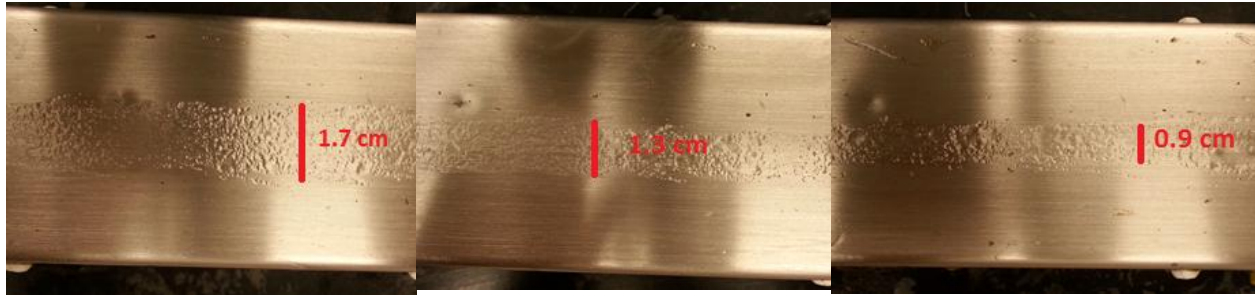
Lamella width is another characteristic of the impingement that is important for the productive coating. In order to study the effects of surface speeds on liquid dimensions, lamella width was measured for 6 different surface velocities. The jet velocity is 5.5 m/s. Lamella is noted to get thinner as surface speed increases.



$$V_{surface} = 5.4 \frac{m}{s}$$

$$V_{surface} = 9.3 \frac{m}{s}$$

$$V_{surface} = 13.42 \frac{m}{s}$$



$$V_{\text{surface}} = 15.91 \frac{\text{m}}{\text{s}}$$

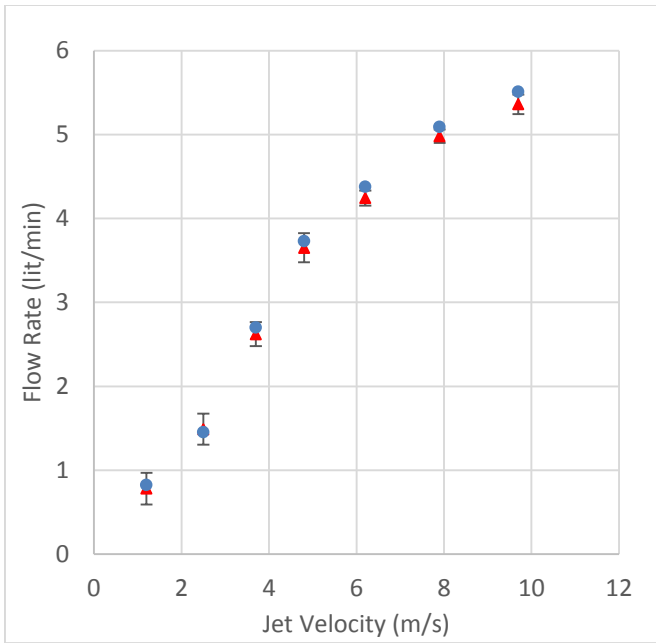
$$V_{\text{surface}} = 18.8 \frac{\text{m}}{\text{s}}$$

$$V_{\text{surface}} = 21.7 \frac{\text{m}}{\text{s}}$$

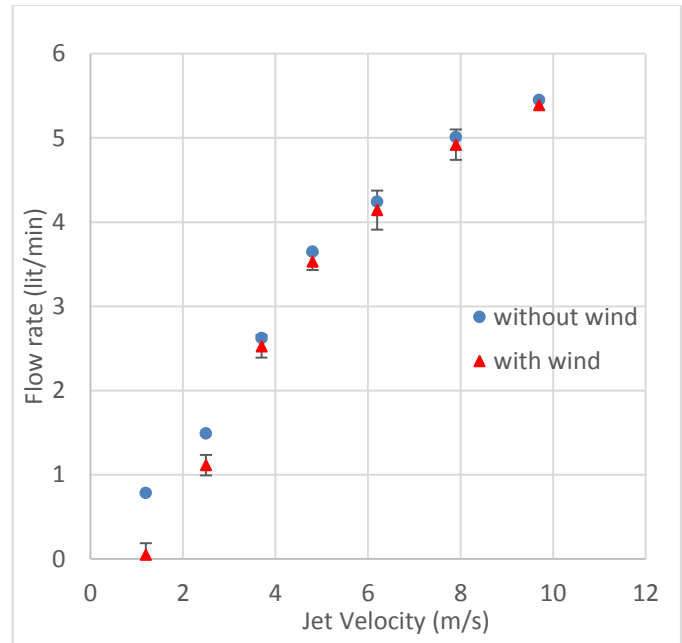
Figure 3-10 Lamella width variation with surface speed at constant jet velocity

### 3.4 Wind Tunnel

In air-blast atomizers, it is really hard to get the sprayed droplets to the rail as they are significantly deflected by cross wind. Although a steady liquid jet is less prone to deflection, this problem still remains. Thus, last step is to study the effects of cross wind. For this purpose, the nozzle was installed in a wind tunnel that had the ability to produce laminar wind up to 20 m/s. The distance from tip of the nozzle to surface is 7.6 cm, and the distance considered for deflection is 3.8 cm, which is half of the field rail width. Tests were conducted for two wind speeds: a medium speed (8.3 m/s) and a high speed (19.9 m/s). The flow was measured when the wind was present and when it was not. At lower wind speeds, around 8.3 m/s, the deflection is negligible and a similar jet to that without a cross wind is expected. However, for higher speeds, the deflection is significant, particularly at low jet velocities. Figure 3-11 shows the flow rate for both wind speeds. Figure 3-12 shows the deflection caused by cross wind for four jet velocities. For all images of figure 3-12, the nozzle back pressure, i.e. jet velocity, is increasing while wind speed is constant.

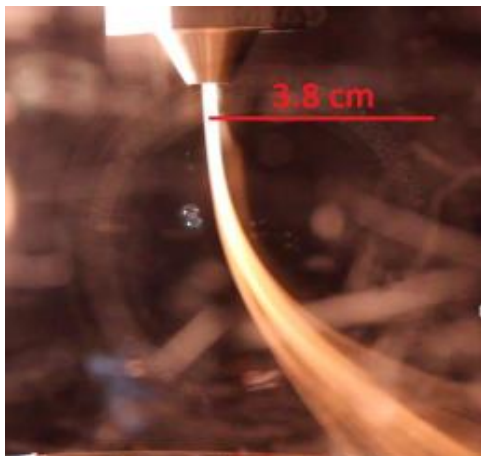


wind speed:8.3 m/s

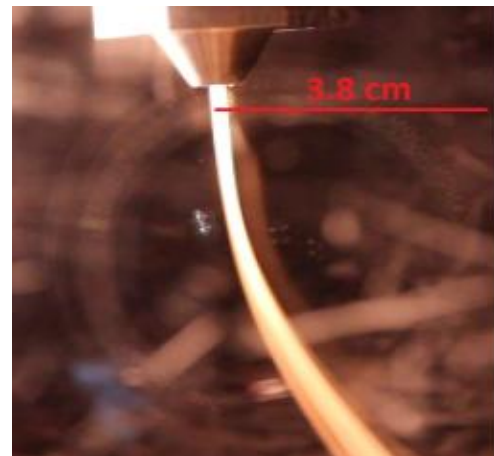


wind speed:19.9 m/s

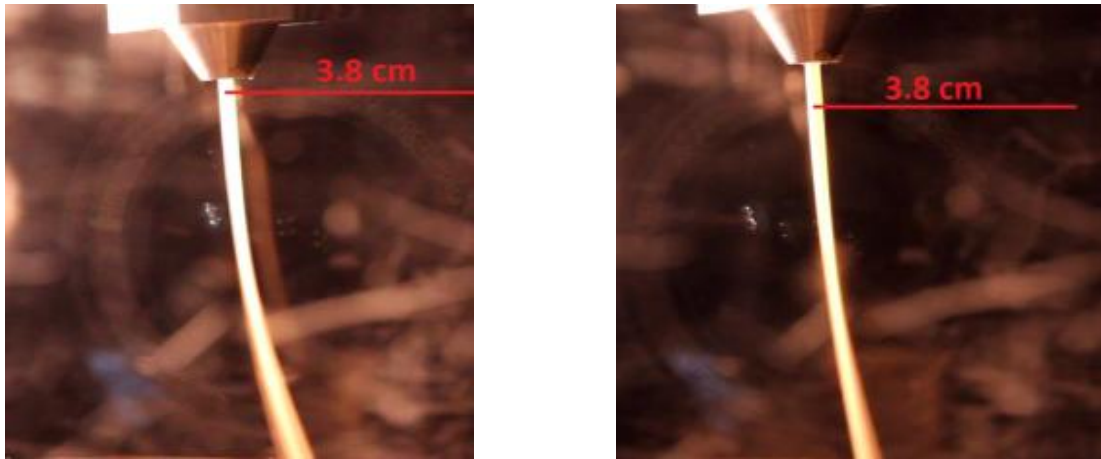
Figure 3-11 Flow rate as a function of jet velocity for different wind speeds



$$V_{\text{jet}} = 1.9 \frac{m}{s}$$



$$V_{\text{jet}} = 3.1 \frac{m}{s}$$



$$V_{jet} = 4.7 \frac{m}{s}$$

$$V_{jet} = 5.9 \frac{m}{s}$$

Figure 3-12 Deflection of ALLEVIATE® steady jet for different jet velocities, wind speed is 19.9 m/s and flows from left to right.

To summarize it, LB Foster desired flow rate is 3 lit/min. Based on Figure 3-5, 3 lit/min flow rate requires about 23 psi nozzle back pressure, or 4.1 m/s jet velocity, with 2.1 mm orifice diameter. Figure 3-7 demonstrates that for jet velocity of 4.1 m/s, deposition occurs for surface speeds lower than 18 m/s. Thus, it is concluded that higher surface speeds lead to splash and waste of materials. Finally, Figure 3-9 shows that cross wind, even with 19.9 m/s speed, cannot deflect the liquid jet more than 3.8 cm, which is the maximum allowable distance that liquid jet can deflect without leaving the surface.

## Chapter 4 : Newtonian Suspension Jets Impingement

The following chapter studies the fundamentals of how steady liquid impinges on a moving surface if particles are added. For this purpose, particle are dispersed in Newtonian fluids. Behaviors of Newtonian liquid jets are well described and any change in behavior can be concluded from particle addition. Keshavarz et al. [13] observed that for a liquid jet impingement on a moving surface, six parameters play a key role in determining the splash threshold: Jet-surface relative velocity ( $V_{rel}$ ), jet diameter ( $D$ ), viscosity ( $\mu$ ), density ( $\rho$ ), surface tension ( $\sigma$ ), and surface roughness ( $\epsilon$ ), yielding the following three dimensionless numbers:

$$Re_{rel} = \frac{\rho V_{rel} D}{\mu} \quad (4 - 1)$$

$$We_{rel} = \frac{\rho V_{rel}^2 D}{\sigma} \quad (4 - 2)$$

$$\text{relative roughness} = \frac{\epsilon}{D} \quad (4 - 3)$$

Once particles are added, two more additional dimensionless numbers appear: Stokes number, associated with mean particle size, and volume fraction:

$$Stk = \frac{t_p}{t_f} \quad (4 - 4)$$

$$\varphi : \text{Volume fraction} \quad (4 - 5)$$

Where  $t_p$  is the characteristic time of a particle and  $t_f$  is the characteristic time of a flow. The characteristic time of the flow is defined as  $t_f = \frac{D_{jet}}{V_{jet}}$ . The characteristic time of the particle can be defined as  $t_p = \frac{(\rho_p - \rho_l) d_p^2}{18 \mu_l}$ ; where  $\rho_p$  is the particle density,  $d_p$  is the particle diameter,  $\rho_l$  is the

liquid density, and  $\mu_l$  is the liquid viscosity. If we can keep all first three dimensionless numbers constant, every change in the outcome of jet impact can be attributed to  $\varphi$  and  $Stk$ . In the same experimental conditions,  $V_{jet}$ ,  $V_{surface}$ ,  $D_{jet}$ , and  $\epsilon$  are unchanged. Depending on the glycerin percentage, the liquid test density can be varied from  $0.998 \times 10^3 \frac{kg}{m^3}$  (100% water) to  $1.252 \times 10^3 \frac{kg}{m^3}$  (100% glycerin).

Rheological data also shows that for low concentrations studied, suspensions remain Newtonian, as presented in Figures 4-2 and 4-3. Only viscosity increases when particles are present. To match the viscosity, the glycerin percentage for suspension base liquid was chosen slightly smaller, as presented in Table 1, to allow for this viscosity increase. Therefore, all governing parameters associated with bulk flow (fluid inertia, surface tension and viscous force) were kept constant. Figure 4-1 shows the contact angle measured for suspensions.

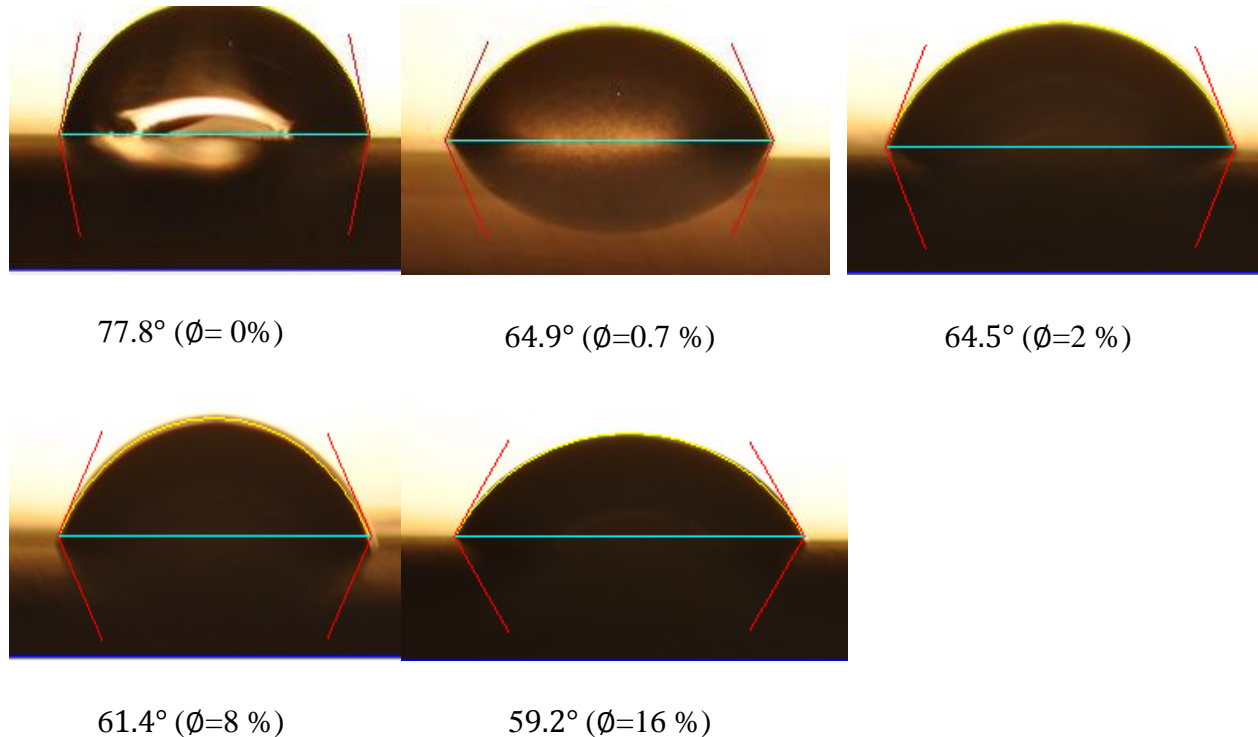
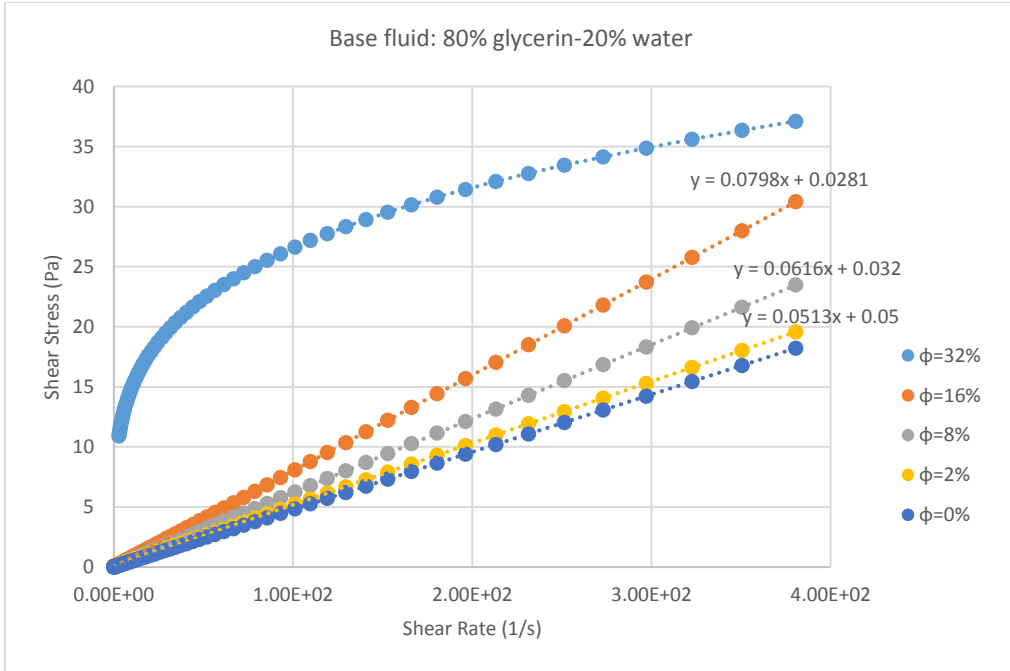


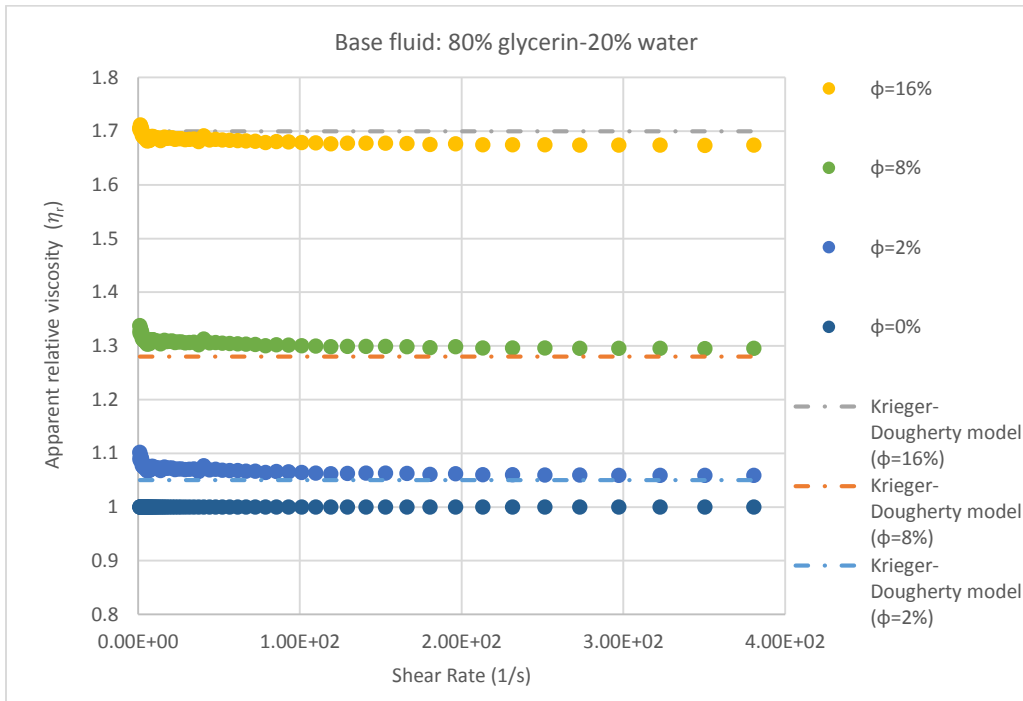
Figure 4-1 Contact angle as a function of suspension volume fraction

Figures 4-2 and 4-3 show the rheological behavior when particles are added to water-glycerin solutions. A model from literature for Newtonian suspensions, namely the Krieger-Dougherty ( $\eta_r = (1 - \frac{\varphi}{\varphi_m})^{-[\eta]\varphi_m}$ ), was fitted to the data. This model predicts the dependence of suspension effective viscosity on shear rate as a function of volume fraction. The suspension viscosity is often written in the form of  $\eta_s = \eta_r(\varphi) * \eta_0$ . Maximum particle packing fraction,  $\varphi_m$ , and intrinsic relative viscosity,  $[\eta]$ , are considered to be fitting parameters, which are mainly functions of the shape of a single particle and particle size distribution [32].  $\varphi_m$  is slightly bigger for poly-disperse particles, because smaller particles can fit in the space between larger ones.

Nine rheological tests with different volume fractions, only three of which are shown in Figures 4-2 and 4-3, for both hollow glass bead and polyester bead suspensions were conducted. After matching Krieger-Dougherty model with all nine data-set for shear rates higher than  $100s^{-1}$ , the fitting parameters were estimated to be  $\varphi_m = 0.67 \pm 0.071$ ,  $[\eta]\varphi_m = 1.94 \pm 0.206$  for glass bead suspensions, and  $\varphi_m = 0.62 \pm 0.064$ ,  $[\eta]\varphi_m = 2.11 \pm 0.21$  for polyester suspensions, respectively. It is estimated that shear rate at impingement point is much greater than  $100s^{-1}$ .



(a)



(b)

Figure 4-2 Rheology test for glass beads suspension: (a) shear stress vs shear rate, (b) relative viscosity ( $\eta_r$ ) vs shear rate

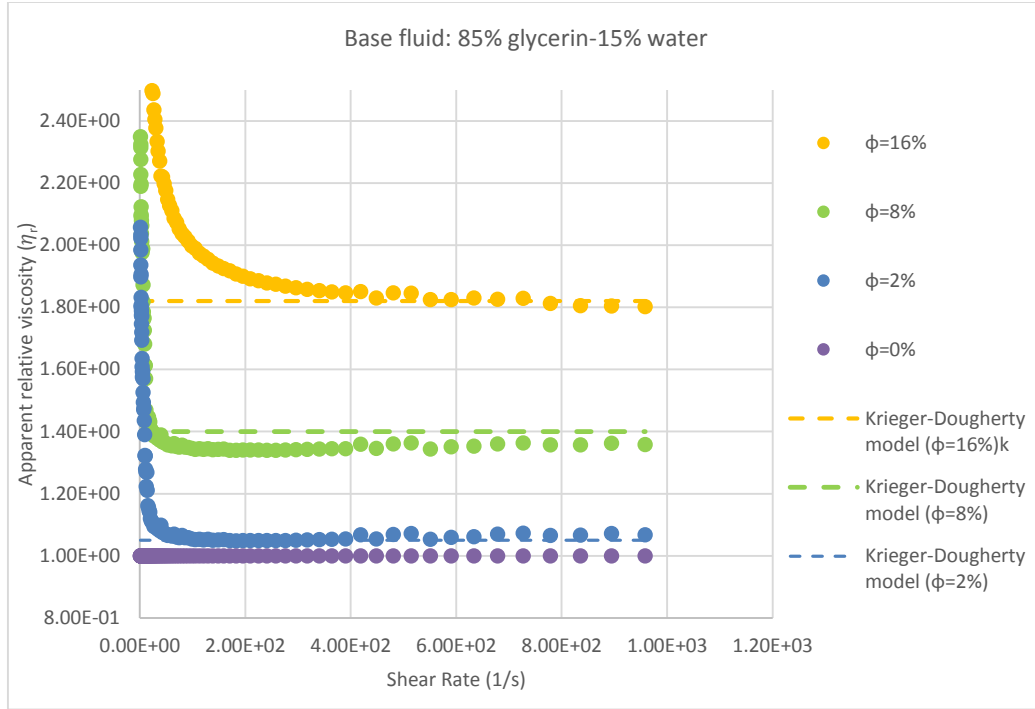


Figure 4-3 Rheology test for polyester suspension: relative viscosity ( $\eta_r$ ) vs shear rate

## 4.1 Glass Bead Suspensions

Hollow glass spheres were chosen with average size of  $15 \mu\text{m}$ , standard deviations from their mean size of 8% to 12%, and density of  $(1.1 \pm 0.05) \times 10^3 \frac{\text{kg}}{\text{m}^3}$ . Figure 4-4 illustrates the discharge coefficient through a circular orifice nozzle. The actual flow rate is small at lower Reynolds number and increases significantly for higher Reynolds number. The reason being the flow has higher shear viscosity at lower Reynolds number, resulting in huge viscous losses through the orifice. This data were gathered for four different mixtures of water-glycerin solutions (GW70, GW75, GW80 and GW85), where 80% glycerin-20% water solution is denoted as GW80 here. The discharge coefficients are close for both cases and the slight difference could be caused by experimental error. Thus, the addition of small particles does not affect the flow behavior within the nozzle.

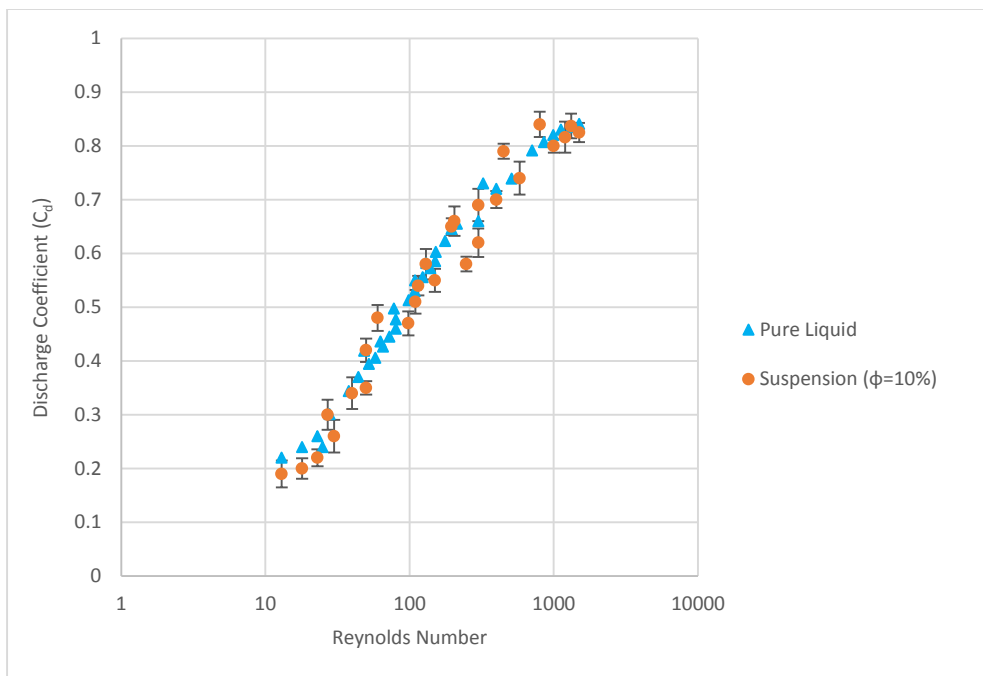


Figure 4-4 Discharge coefficient as a function of Reynolds number

Test liquids were applied to the surface for different surface speeds and jet velocities. High speed spinning disk apparatus was used for this impingement. Figure 4-5 shows the time series of jet impact on a moving surface. For same conditions, a pure liquid jet splashes while suspension jet deposits smoothly on the surface. This figure clearly demonstrates that splash can be suppressed by dispersing very small particles at low concentrations in a Newtonian liquid. The surface is moving from left to right at  $14.76 \text{ m.s}^{-1}$ .

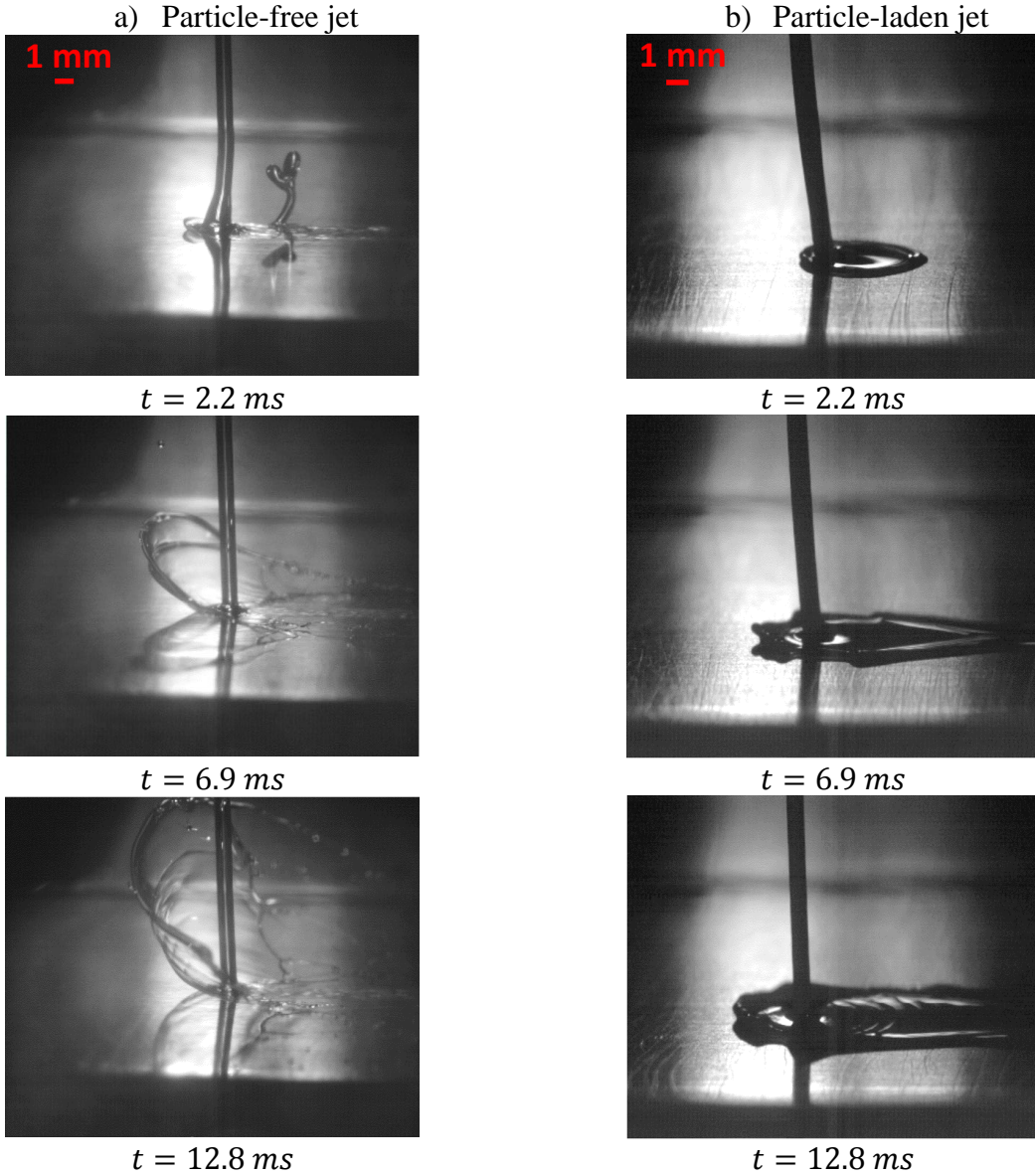


Figure 4-5 Time series of jet impact on a moving surface: a) particle-free liquid jet, b) particle-laden jet with volume fraction of 10%. The substrate is moving from left to right at 14.76 m/s. Other test conditions: jet velocity is 8.3 m/s, solution is GW75 (viscosity of 0.0287  $mPa \cdot s$ ), jet diameter is 1.3 mm, and the ambient pressure is 101 kPa.

Contrary to the different splashing and spreading behaviors, the shapes of the lamella are similar. Lamella dimensions (width, thickness, and radius) were measured for both cases and were almost equal. However, a wave form instability, shown in Figure 4-6, was observed downstream of the deposited lamella, which was not seen previously. It is speculated the solid spheres in the jet are responsible for the instability.

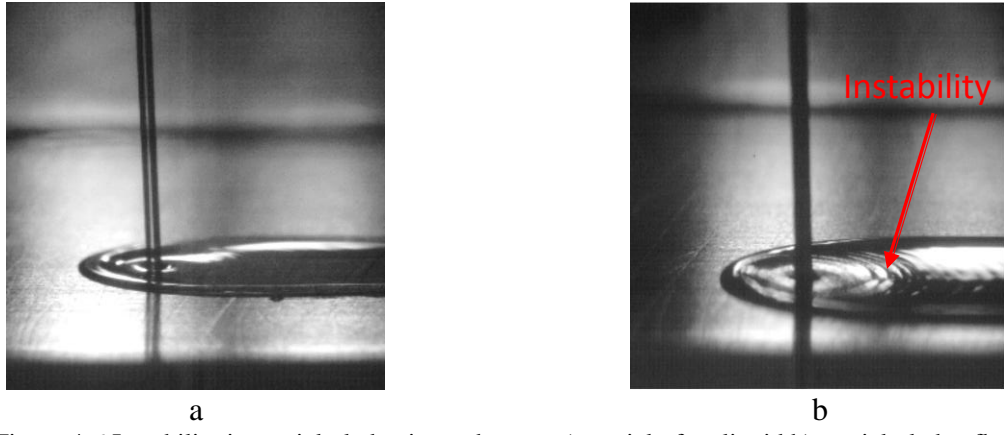
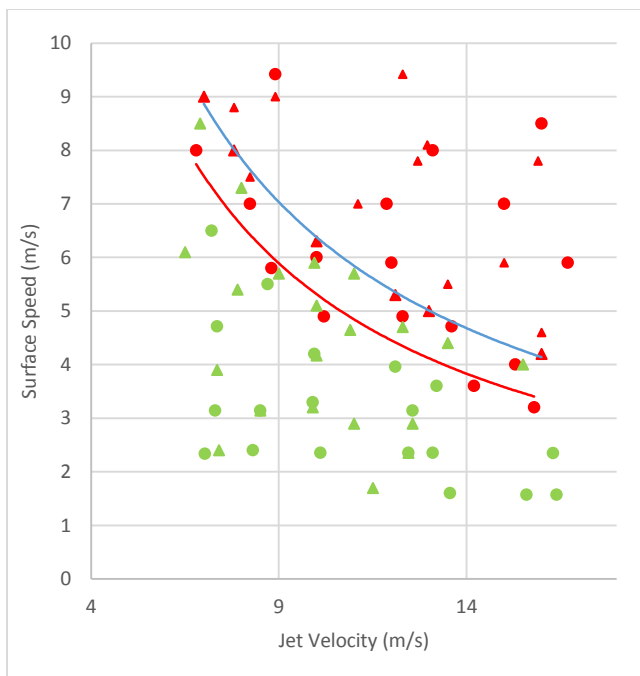


Figure 4-6 Instability in particle-laden jet, red arrow a) particle-free liquid b) particle-laden flow

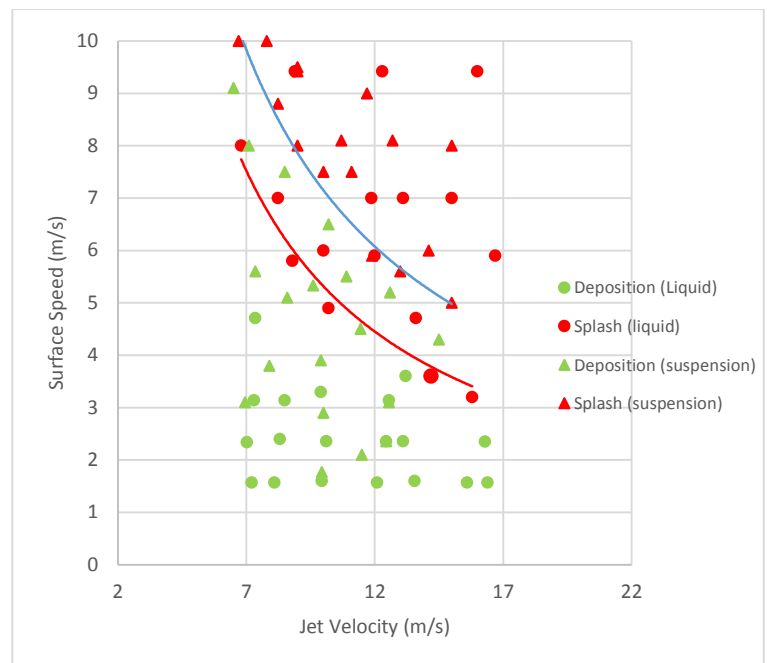
Figures 4-7 and 4-8 show splash thresholds for suspensions with different concentrations.

All tests were done for 1.3 mm orifice diameter. The left figures show the data for 5% suspensions and right figures are for 10% suspensions. The splash threshold was quantified for each case. Experiments were repeated to ensure repeatability of the phenomena near the thresholds, where transition from deposition to splash occurs. An algorithm was used to set the best line based on minimizing the root mean square (RMS) error. To confirm the accuracy and repeatability, one line was passed through the deposition points near the threshold, another line was passed through the splash points, and the average line was chosen as the final splash boundary in all of the following graphs.

Figures 4-9 and 4-10 display the same data but as a function of dimensionless numbers, jet Reynold number ( $Re_{jet} = \frac{\rho V_{jet} D}{\mu}$ ) and jet Weber number ( $We_{jet} = \frac{\rho V_{jet}^2 D}{\sigma}$ ). Each line of the data-set was obtained by changing solution properties, i.e. viscosity and density, or orifice diameter. Each point along the line is for particular jet velocity; as we move along the line, the jet velocity rises. The graphs were plotted

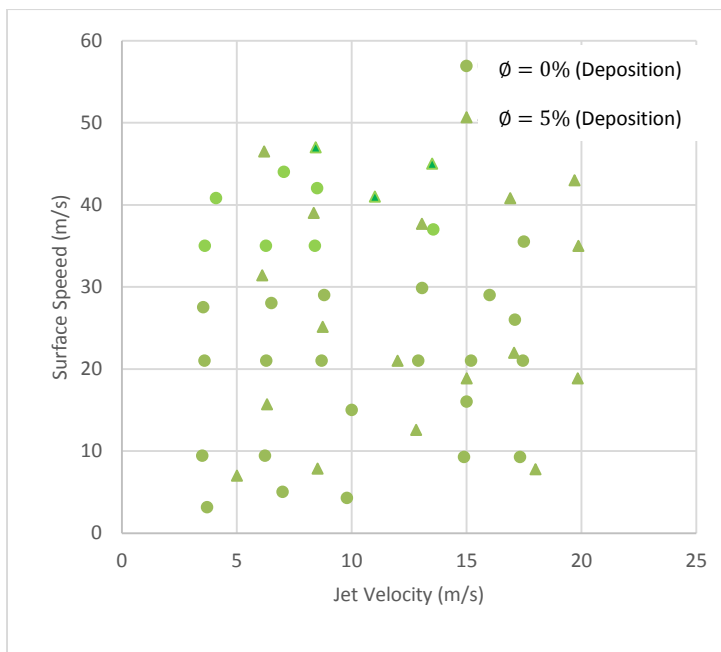


a) 5% suspension

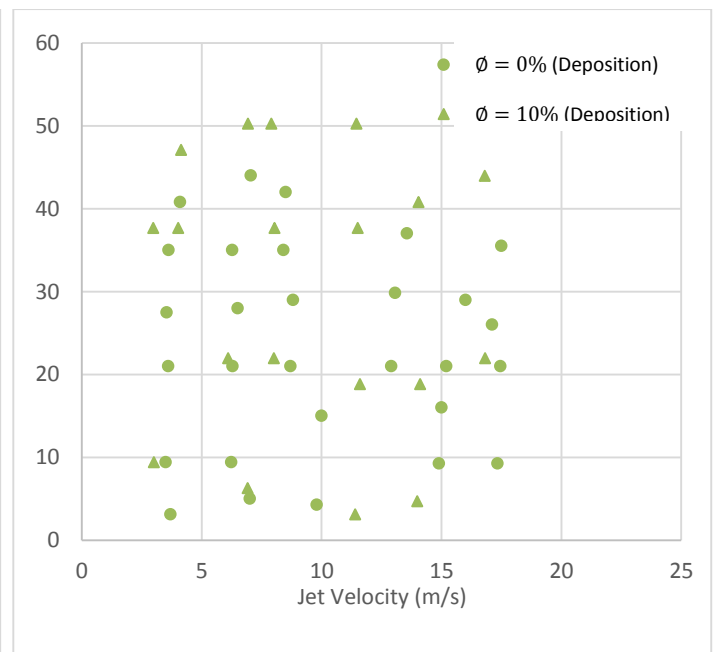


b) 10% suspension

Figure 4-7 Splash-deposition map regime for 65% glycerin-35% water. Red lines show the threshold for particle-free jets and blue lines show the threshold for particle-laden jets.



a) 5% suspension



b) 10% suspension

Figure 4-8 Splash-deposition map regime for 85% glycerin-15% water.

for constant surface speeds, surface roughness, and particle size. Splash boundaries were identified for all three volume fractions, but data for 5% volume fraction is not shown for graph clarity.

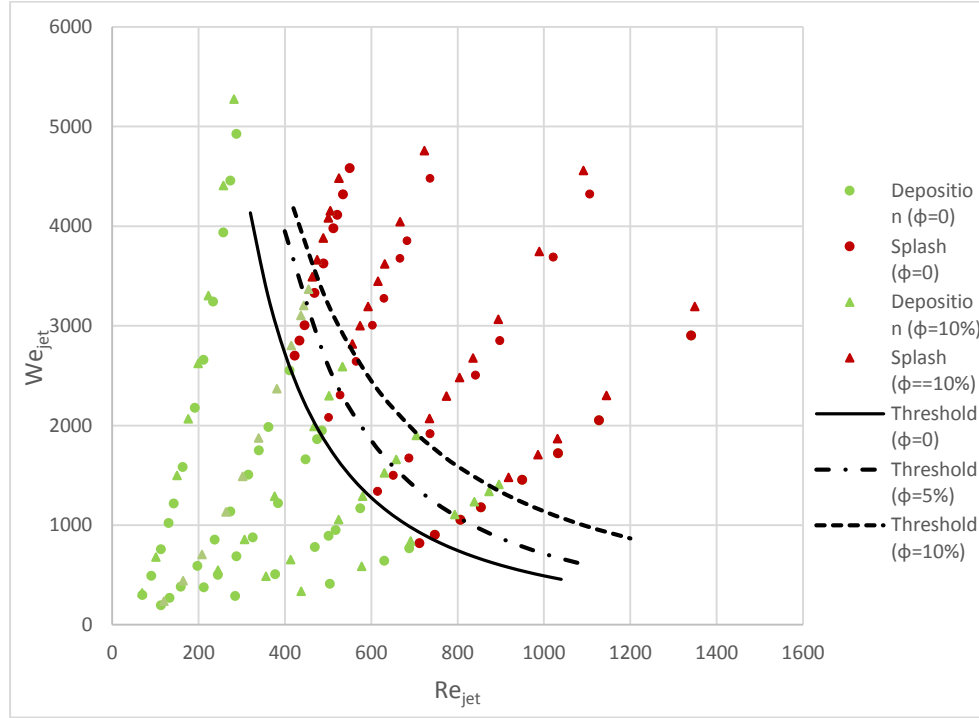


Figure 4-9 Splash regime map for particle-laden jet at a constant surface speed of  $14.76 \text{ ms}^{-1}$ . Surface roughness is  $0.15 \mu\text{m}$  and the average particle size is  $15 \mu\text{m}$ .

Splash is suppressed if small particles are added at low concentrations. For instance, in Figure 4-9, at  $We=2000$  Full deposition was achieved for pure liquid at  $Re<480$ ; while this number is  $Re<580$  for 5% volume fraction, and  $Re<690$  for 10% volume fraction. The late splash may be caused by an increase in friction between particles and the substrate surface. After impact, the particles will move within the lamella, whose thickness is  $\sim 70 \mu\text{m}$ . Thus, the particles may touch the surface and increase the friction loss, leading to more energy dissipation. Another possible explanation is that after impact, particles tend to remain in the proximity of the wall, i.e. in the region of higher shear in the flow. Therefore, the layer near the wall becomes rich of particles, whereas the regions further away become depleted. Two things can happen: First, the fluid

elements, which previously tumbled over each other near the wall, should tumble over the solids particles as well. This results in an increase in the shear stress at the wall, which acts as a mechanism to extract kinetic energy. Second, the presence of the particles near the wall may locally increase the surface roughness, i.e. they would stick to the wall with a lower relative velocity to the upper layers motion.

The jet impingement with suspended particles is more likely to splash at higher We and Re numbers. This is consistent with the findings of Moulson and Green [26] for a pure liquid jet. For a particle-laden flows, as well as pure liquids, the threshold is non-linearly dependent on Reynolds number [19]. At small Reynolds number, the jet does not splash regardless of Weber number; while for larger Reynolds, the lamella detachment occurs depending on Weber number.

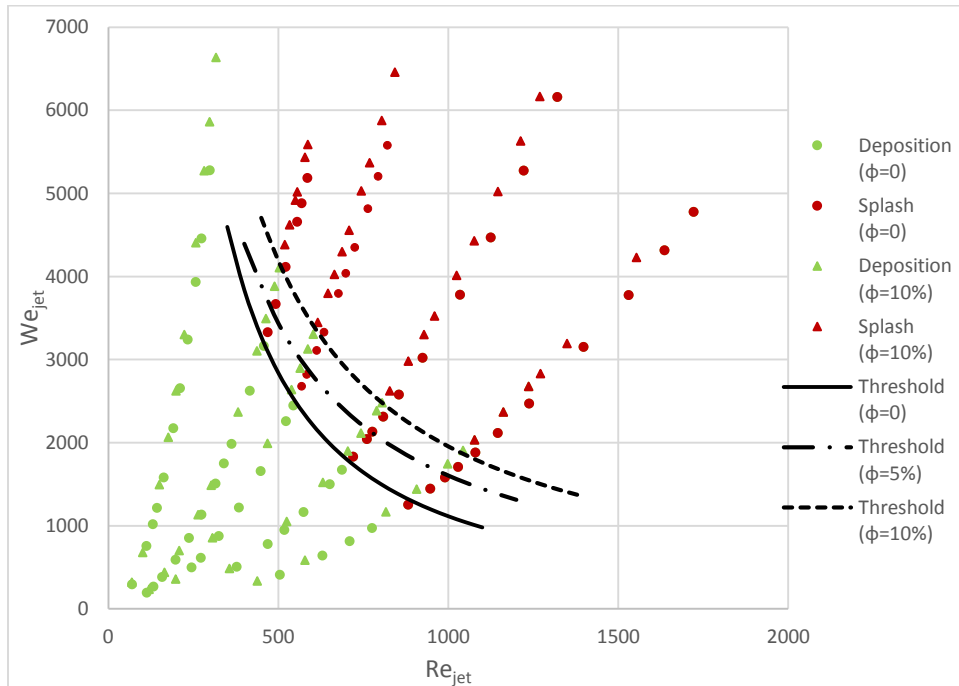


Figure 4-10 Splash regime map for particle-laden jet at a constant surface speed of  $8.71 \text{ ms}^{-1}$ . Surface roughness is  $0.15 \mu\text{m}$  and average particle size is  $15 \mu\text{m}$ .

Figure 4-10 demonstrates the same splash-deposition regime map but for lower surface speed,  $8.71 \text{ m/s}$ . Again, splash was suppressed for particle-laden jet. The boundaries for all three

volume fractions show higher dependence on Reynolds number. At  $We=2000$  full deposition was achieved for pure liquid at  $Re<640$ , for 5% dense particle-laden flow at  $Re<790$ , and for 10% dense particle-laden flow at  $Re<980$ .

To confirm that the experimental results are repeatable, the same splash thresholds as Figure 4-10 but with error bands (shown in blue) are plotted in Figure 4-11. The random inputs of experiments were chosen, and the uncertainties were identified statistically based on the influence of each point error on the splash curve behavior.

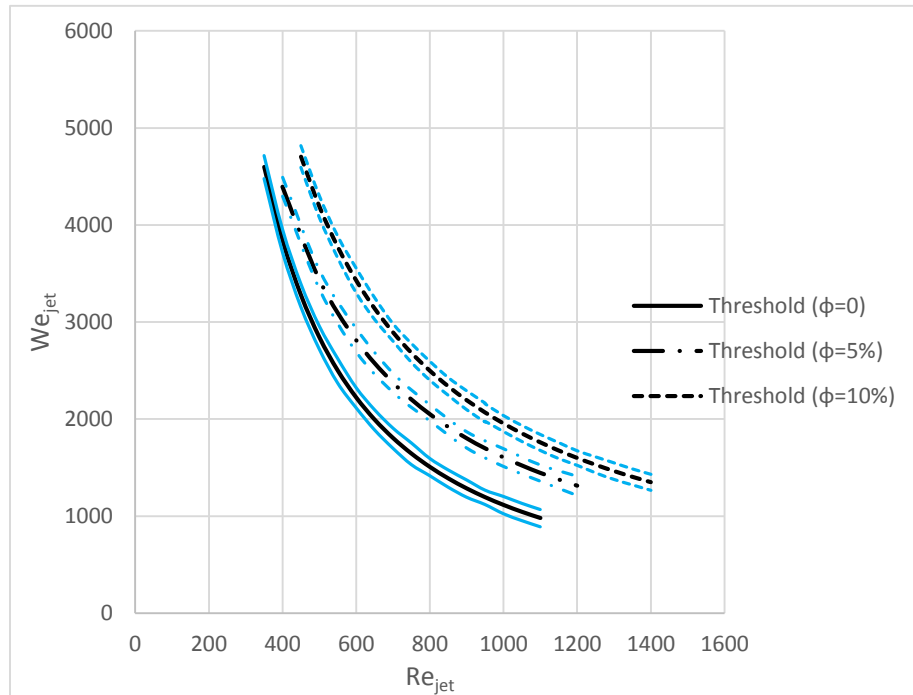


Figure 4-11 Error bands for splash thresholds (blue lines). Test conditions are given in the caption of Figure 4-10.

## 4.2 Polyester Suspensions

Polyester particles were chosen with mean size of  $180 \mu m$ , standard deviations from their mean size of 15% to 25%, and density of  $(1.15 \pm 0.08) \times 10^3 \frac{kg}{m^3}$ . Although the suspended glass

bead jets were stable when impacting the surface, polyester-laden jets showed instability. The instability was observed at nozzle discharge for all jet velocities higher than 4.8 m/s. Figure 4-12 shows the jet instability for different velocities. As we increase the jet velocity or reduce the viscosity, i.e. higher Reynolds number, the instability gets worse.

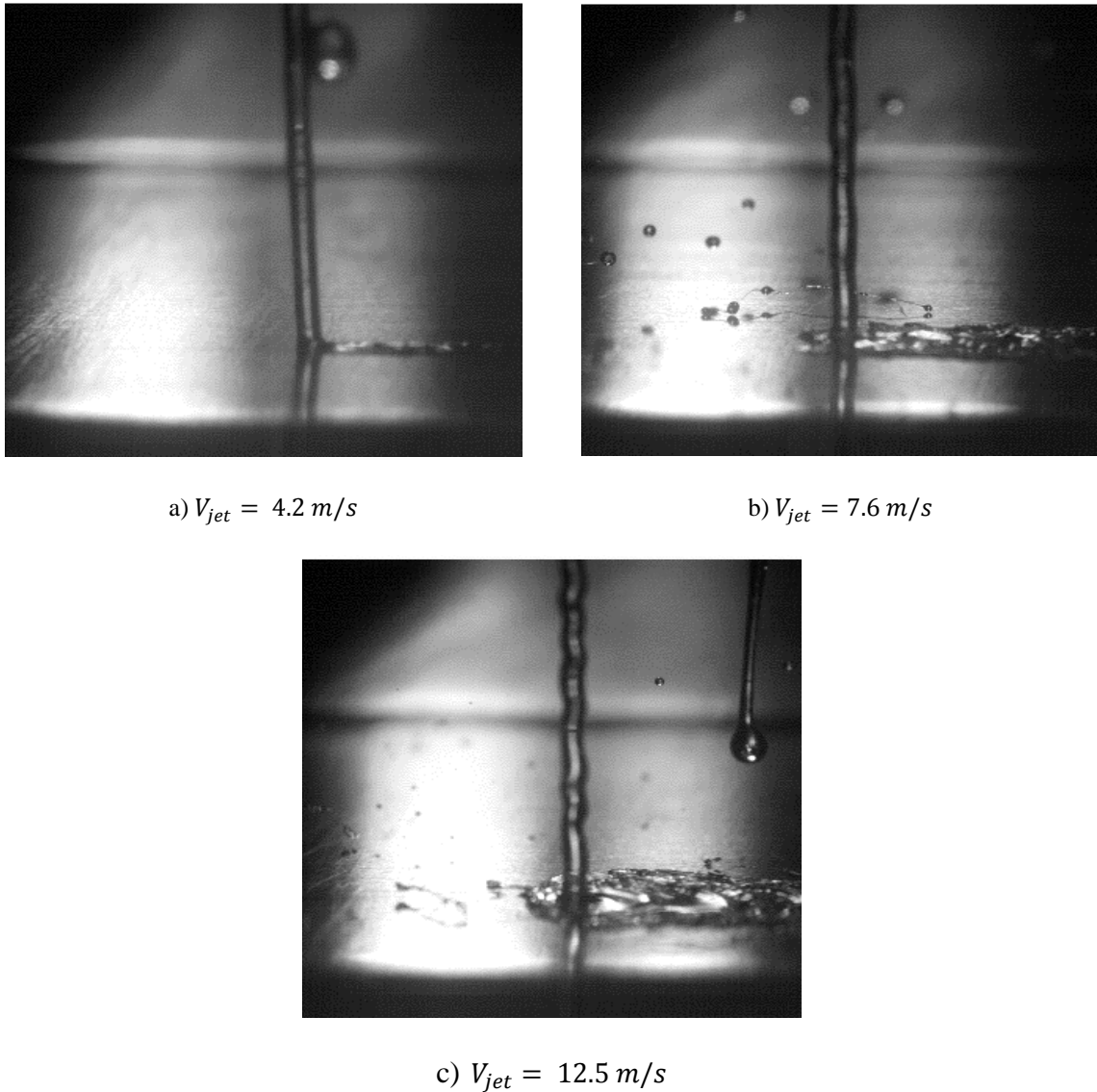


Figure 4-12 Jet instability for different jet velocities

Particle size is a big fraction of jet diameter, thus particles will not respond completely to fluctuations in a flow, particularly at the nozzle exit. To resolve this, a hypodermic tube was attached to the nozzle tip to smooth out the disturbances through nozzle. The length of this tube was estimated by hydrodynamic entrance length in a laminar flow,  $0.05ReD$ . Several experiments suggested that this hypodermic tube does not change the splash-nonsplash boundary.

To confirm homogeneity of the flow, high speed images were captured at nozzle exit. Figure 4-13 verifies that the solution is homogenous and particles are plausibly dispersed in the flow to yield a neutrally buoyant suspension.

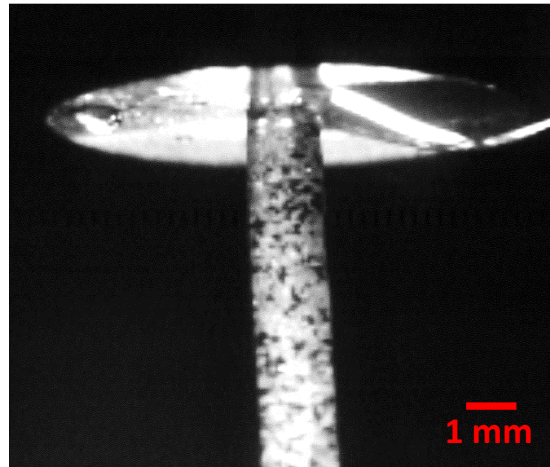


Figure 4-13 Polyester suspension jet at nozzle exit

Accordingly, lamella dimensions were measured for polyester-laden jets impingement and again they were almost equal to the case of pure liquids. However, since polyester particles are larger than the lamella thickness ( $\sim 70 - 100 \mu m$ ), sometimes they are not entirely submerged in liquid.

Figures 4-14 and 4-15 show the splash thresholds for suspension of 10% volume fraction.

Figures 4-16 and 4-17 highlight the splash-deposition map as a function of dimensionless numbers, jet Reynold number and jet Weber number. Based on the Figure 4-16, at  $We=3000$  the pure liquid never splashes when Reynolds number is below 490. However, these values are much smaller for suspensions:  $Re<295$  for 5% volume fraction, and  $Re<245$  for 10% volume fraction. The threshold for 5% volume fraction is much closer to the 10% suspension rather than to the pure liquid. It is speculated that, in the dilute limit the threshold is less dependent on solids concentrations and just the minimum fraction is required to initiate lamella detachment.

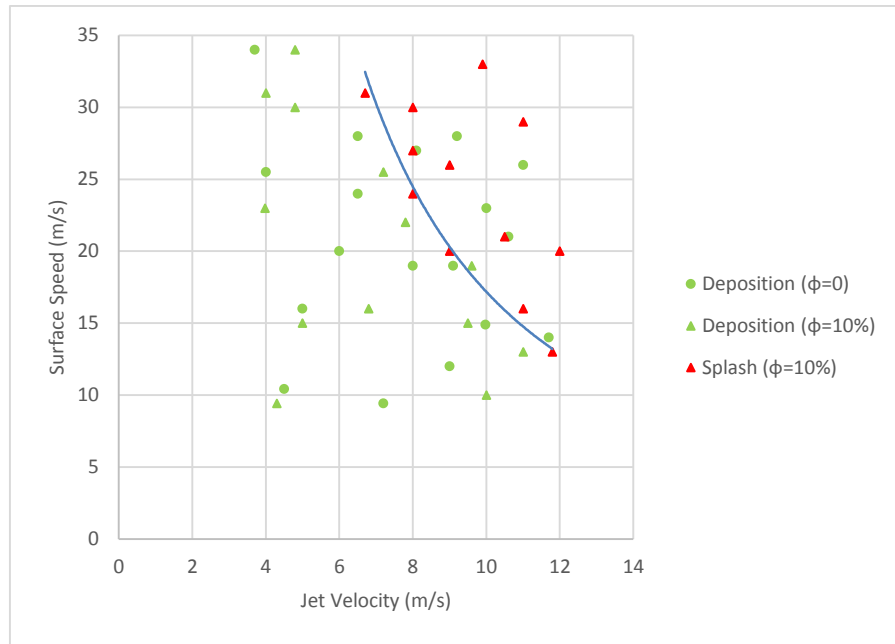


Figure 4-14 Splash-deposition map regime for 85% glycerin-15% water. Blue line shows the threshold for large particles in a jet.

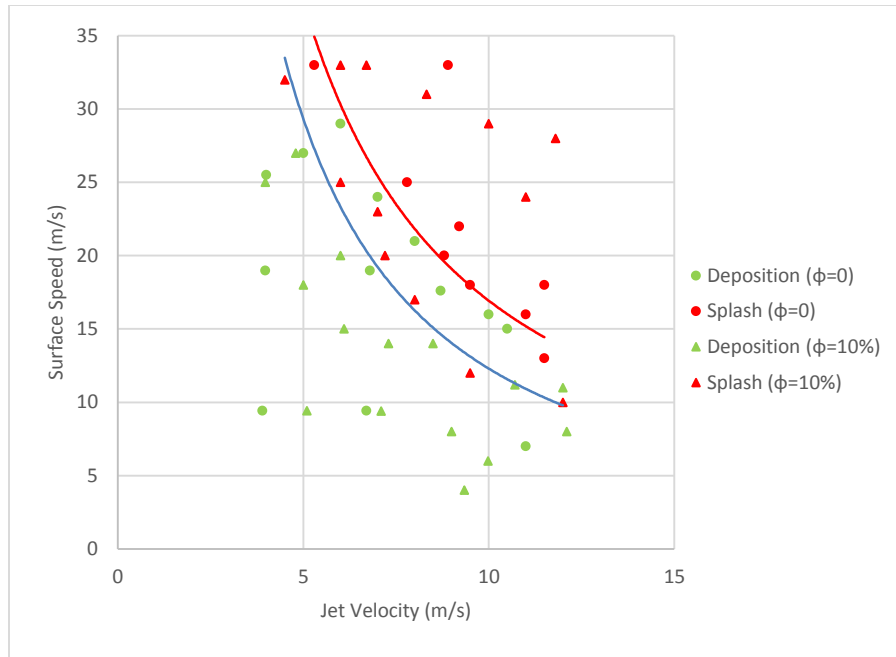


Figure 4-15 Splash-deposition map regime for 75% glycerin-25% water. Red lines show the threshold for particle-free jets and blue lines show the threshold for particle-laden jets.

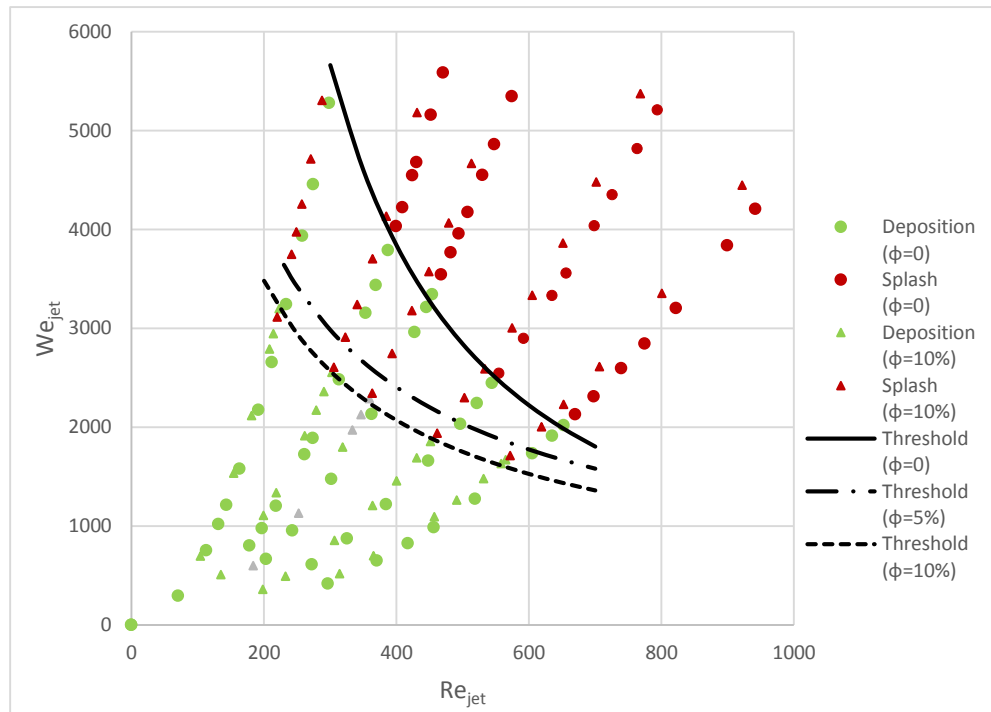


Figure 4-16 Splashing regime map for particle-laden jet at a constant surface speed of  $8.71 \text{ ms}^{-1}$ . Surface roughness is  $0.15 \mu\text{m}$  and average particle size is  $180 \mu\text{m}$ .

In addition to significant changes in splash thresholds, dependence of each curve on Reynolds and Weber numbers needs to be addressed. For pure liquids and glass beads, the boundaries are mostly functions of Reynolds number at elevated Weber number. However, for polyester particles the boundary shows high dependence on Weber as well, particularly at low Reynolds numbers. Using the Weber number as a criterion to determine the splash threshold was first proposed by Peters et al. [17]. He performed an energy balance at the particle level and concluded that the particle Weber number,  $\frac{\rho_p r_p U^2}{\sigma}$ , is the key parameter for dense suspension droplets.

Experiments were conducted for additional surface speeds and the same trends were observed. Figure 4-17 highlights the data for larger surface roughness. Likewise, the error bands for polyester beads are presented in Figure 4-18, shown in blue lines. The trend of thresholds is consistent with previous findings, expecting to have more splash by increasing the surface roughness from  $0.15 \mu m$  to  $0.3 \mu m$  [27]. However, this change of roughness slightly affected the splash threshold for particle-laden jets. For example, for pure liquids, the difference between thresholds for smooth and rough surfaces at  $Re = 400$  is about  $We = 870$ ; while this value is only  $We = 190$  for 10% volume fraction. The reason for this may be associated with difference in nature of splash between particle-laden jets and liquid jets. For former, splash may occur through particle ejection or particles may initiate the detachment. Peters et al. [17] also found that the threshold of dense drop suspensions did not depend on the roughness of the glass substrate. However, it has been well documented that the roughness has huge effects on pure liquid drop and jet impacts.

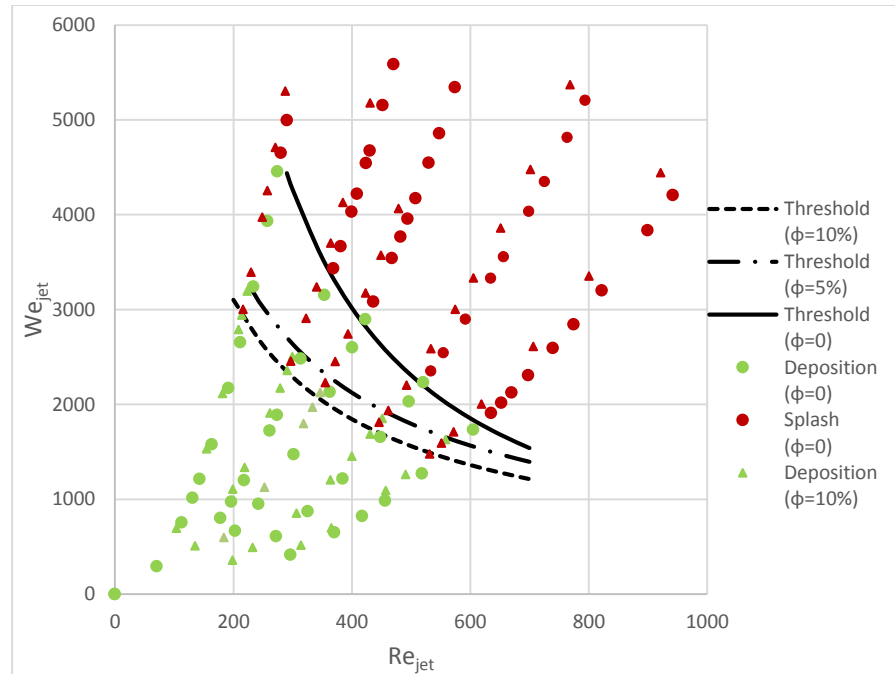


Figure 4-17 Splashing regime map for particle-laden jet at a constant surface speed of  $8.71 \text{ ms}^{-1}$ . Surface roughness is  $0.3 \mu\text{m}$  and average particle size is  $180 \mu\text{m}$ .

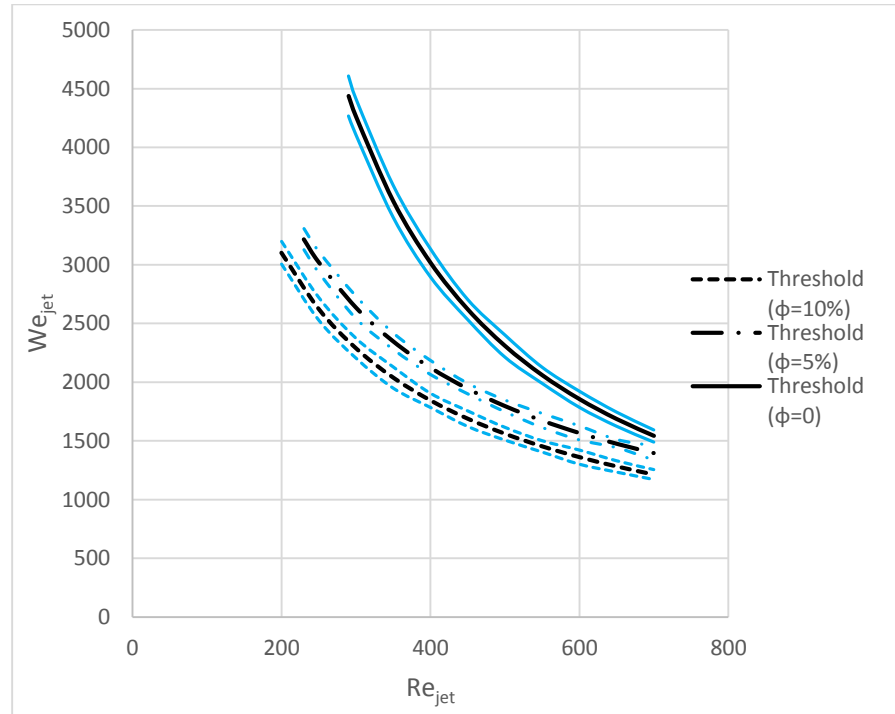


Figure 4-18 Error bands for splash thresholds (blue lines). Test conditions are given in the caption of Figure 4-17.

### 4.3 A Model for Jet Impingement

Bird et al. [13] developed a model for liquid drops impact on a moving substrate. Keshavarz et al. [19] redefined this model for liquid jets. In this study, the same approach, but with different arrangements, will be used to modify the Bird's model for liquid jets. The experimental data will be fitted to the model and fitting parameters are found to be dependent on both mean particle size and volume fraction.

Bird et al. [13] proposed that only when the kinetic energy of a drop is much greater than the surface energy, the liquid film becomes unstable and splash occurs. Drop kinetic energy is scaled as  $\rho(V_l - V_t)^2 L^2 h$  and surface energy is scaled as  $\sigma h L$ . Thus, splash occurs if

$$\frac{\rho(V_l - V_t)^2 L}{\sigma} > C \gg 1 \quad (4-6)$$

Where  $V_l$  is the lamella velocity,  $V_t$  is the tangential velocity (surface velocity in this study), and  $L$  is the lamella length (see Figure 4-19(a)). Several assumptions were made and the values of lamella velocity and length were found to be  $V_l = c_1 R Re^{-1/2}$ ,  $L = c_2 V_n Re^{1/2}$ , where  $c_1$  and  $c_2$  are constants, and  $V_n$  is normal velocity. Substituting these values into Eq. 4-6 leads to threshold criterion:

$$WeRe^{\frac{1}{2}}(1 - k \frac{V_t}{V_n} Re^{-\frac{1}{2}})^2 > K \quad (4-7)$$

Same assumptions are made here (see Figure 4-19(b)). Based on the continuity, the volume of region \* is equal to the volume of region \*\* ( $\pi r^2 \delta = \pi((r + l)^2 - r^2)h$ ). Lamella thickness is obtained by momentum boundary layer thickness ( $h = c_1 \sqrt{vt}$ ), where  $c_1$  is a constant of  $ord(1)$  and  $t$  is the time since impact. Different experimental observations suggest that the addition of particles do not change the lamella dimensions of steady liquid jets impingement. Finally, splash occurs

when the lamella gets distinctly separate from the liquid jet. The critical time for splash occurrence is scaled as  $t_c = \frac{\nu}{V_n^2}$ . Through applying these assumptions, we can obtain the lamella velocity

$$V_l(t_c) = l(t_c) = \frac{rV_n^2}{6c_1\nu} = c_2 V_n Re_{jet} \quad (4 - 8)$$

Where  $c_2$  is a constant of  $\text{ord}(1)$ , and  $Re_{jet} = \frac{RV_n}{\nu}$ . Weber number is defined based on the jet radius

and velocity ( $We_{jet} = \frac{\rho V_{jet}^2 R}{\sigma}$ ). Substituting into Eq. 4-6 leads to an expression for threshold

$$We_{jet} \cdot Re_{jet}^2 \left( \frac{1}{6} - k \frac{V_t}{V_n} Re_{jet}^{-1} \right)^2 > K \quad (4 - 9)$$

Where  $k \sim 1/c_1$  is a constant of  $\text{ord}(1)$ , and  $K$  should be much greater than one. In Eq. 4-9, all parameters are positive except  $V_t$ , which is positive if lamella moves in the same direction of surface and negative if lamella moves in the opposite direction (Bird et al. [13]). Figure 4-20 shows

the data mapped onto a new graph,  $\frac{We_{jet} Re_{jet}^2}{K}$  as a vertical axis and  $\frac{V_t}{V_n} Re_{jet}^{-1}$  as a horizontal axis.

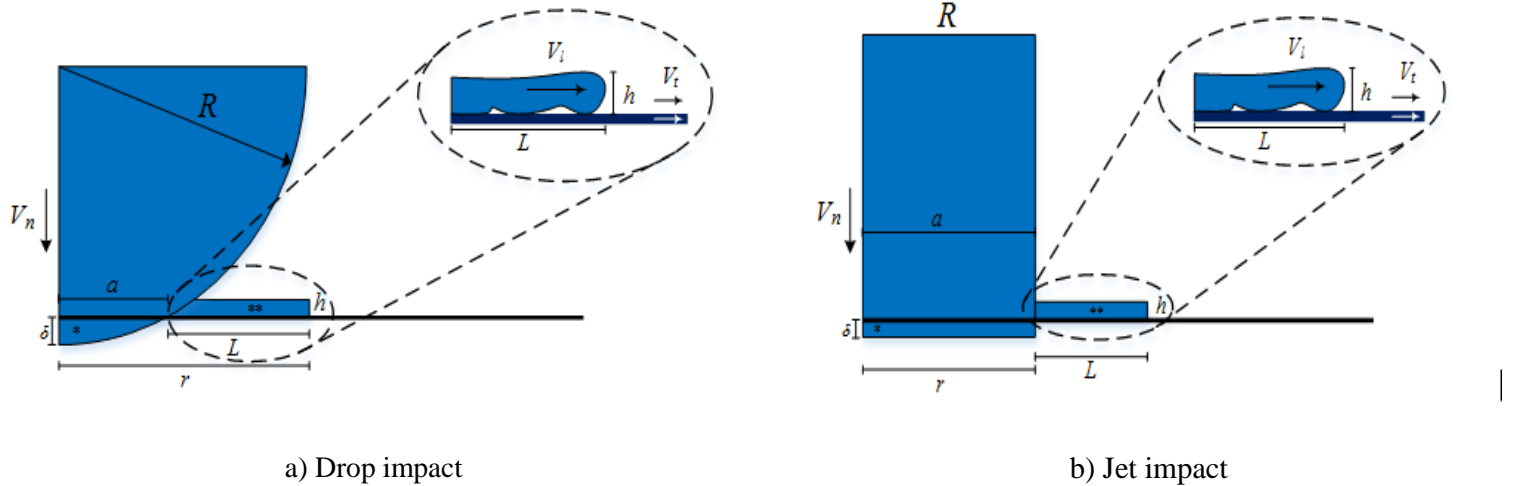
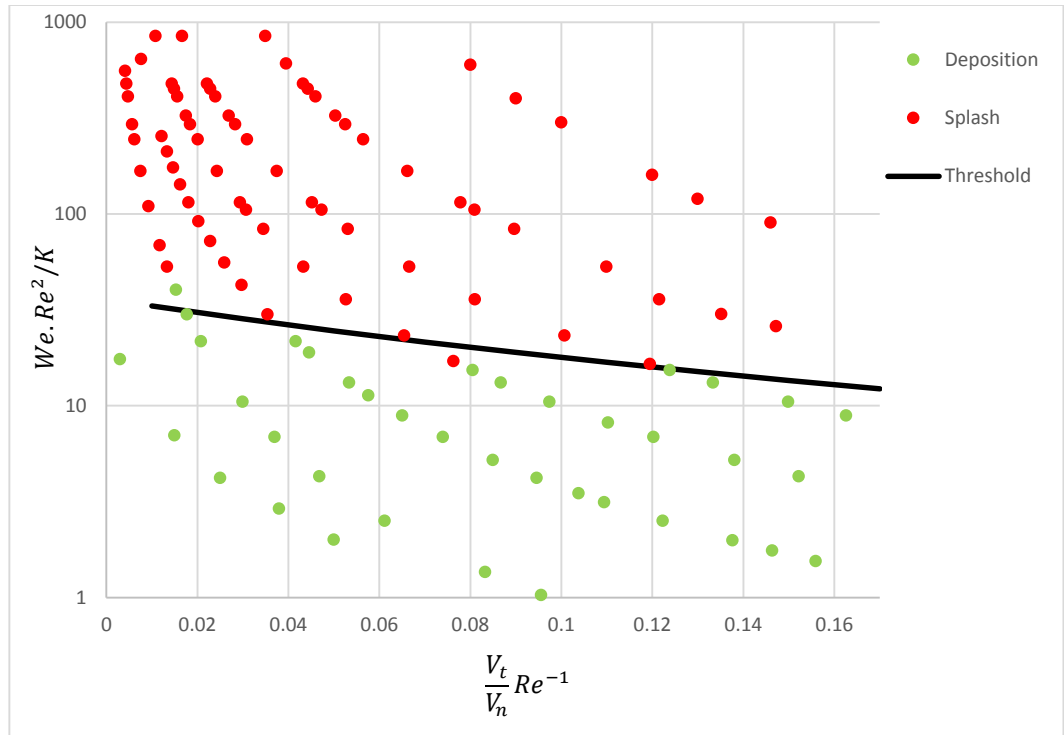
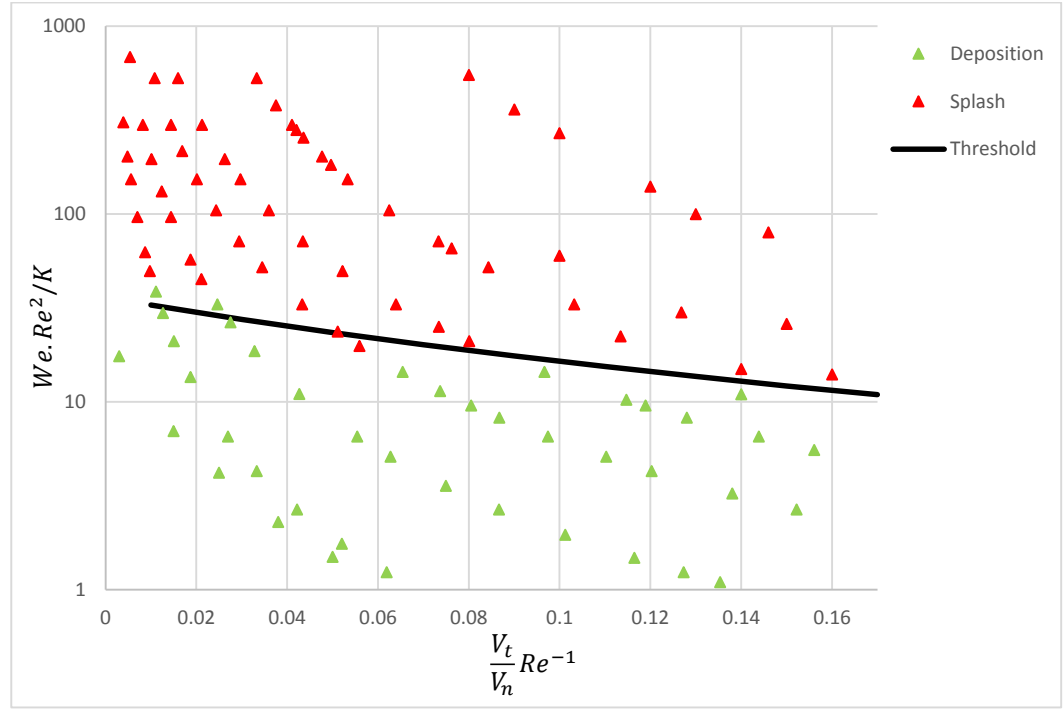


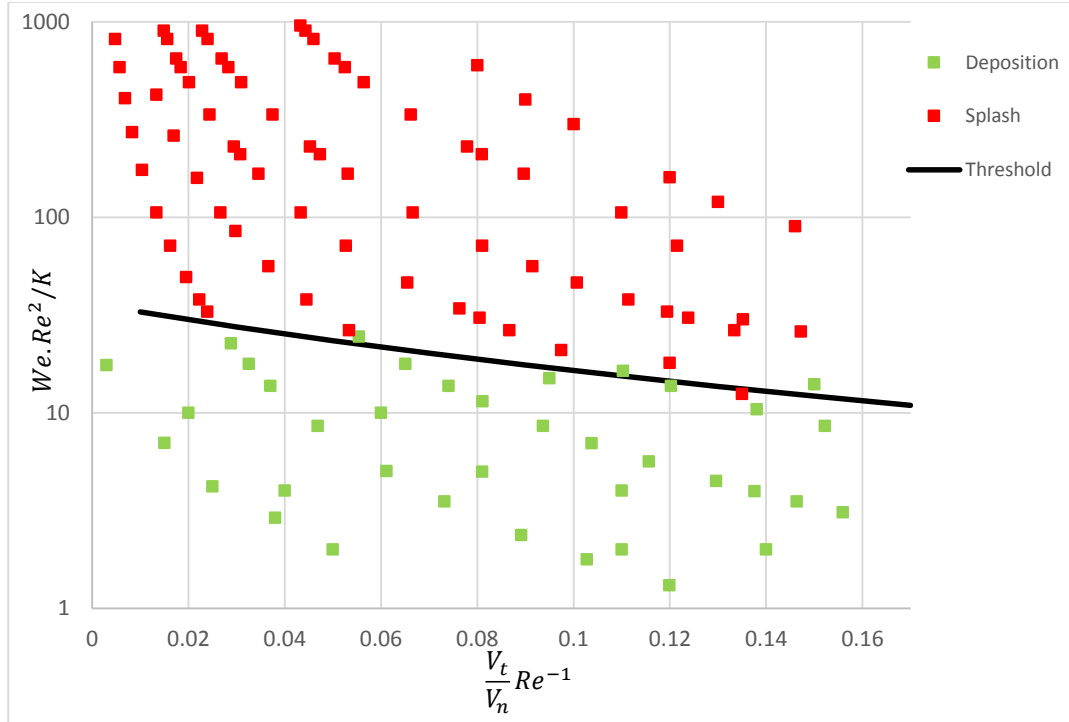
Figure 4-19 Model proposed for drop impact and jet impingement.  $V_n$  is a normal velocity and  $V_t$  is a tangential velocity



a) Pure liquid ( $\varphi = 0$ ), smooth surface,  $k = 0.8$  and  $K = 5.22 \times 10^5$



b) Glass bead suspension ( $\varphi = 10\%$ ), smooth surface,  $k = 0.9$  and  $K = 8.51 \times 10^5$



c) Polyester suspension ( $\varphi = 10\%$ ), smooth surface,  $k = 0.9$  and  $K = 2.61 \times 10^5$

Figure 4-20 Comparison of experimental results with model predictions. Points are the data from experiments and threshold lines are fitted from jet impact modeling for given conditions.

The eight sets of experimental data were fitted to the model, only three of which are shown above. Fitting parameters ( $k$  and  $K$ ) were found for various volume fractions and particle sizes (Table 4-1). A computer-based code was written to find the best values of  $k$  and  $K$  based on minimizing the root mean square (RMS) error. Depending on the number of points selected, the error bars for both  $k$  and  $K$  were estimated statistically. The results are consistent with previous studies for different roughness heights, i.e.  $K$  decreases with surface roughness [13,19,28]; however, the authors know of no previous studies to quantify these parameters for Newtonian suspension jets impact.

Table 4-1 Fitted k and K for particle-laden jets impingement for various particle size, volume fraction, and surface roughness

Particle-free liquid			
Volume Fraction (%)	Surface type	k	K
0	Smooth	$0.8 \pm 0.1$	$(5.22 \pm 0.31) \times 10^5$
0	Rough	$1.1 \pm 0.1$	$(3.97 \pm 0.28) \times 10^5$
Glass bead suspensions			
5	Smooth	$1 \pm 0.2$	$(7.20 \pm 0.39) \times 10^5$
10	Smooth	$0.9 \pm 0.1$	$(8.51 \pm 0.48) \times 10^5$
5	Rough	$1 \pm 0.1$	$(5.53 \pm 0.40) \times 10^5$
10	Rough	$1.3 \pm 0.2$	$(6.37 \pm 0.29) \times 10^5$
Polyester suspensions			
5	Smooth	$0.9 \pm 0$	$(3.55 \pm 0.18) \times 10^5$
10	Smooth	$0.9 \pm 0.1$	$(2.61 \pm 0.18) \times 10^5$
5	Rough	$0.8 \pm 0.1$	$(3.24 \pm 0.25) \times 10^5$
10	Rough	$0.7 \pm 0$	$(2.40 \pm 0.27) \times 10^5$

## **Chapter 5 : Numerical Simulation of a Liquid Jet Impinging on a Moving Substrate**

In this chapter a high-speed steady laminar jet impingement on a fast moving surface is studied numerically. Velocity profiles at different locations, free surface shape, and lamella dimensions (radius, width, and thickness) are presented for various jet and surface velocities, nozzle diameters, and viscosities. The simulation is carried out for Newtonian liquid without any particles.

The impact of a liquid droplet, an area of similar physic, on a flat solid substrate has been studied numerically for a wide range of liquid properties, surface characteristics, and droplet velocities. Bussamnn et al. [33] developed a three-dimensional model for a drop impact on a solid surface. They used the fixed-grid Eulerian model and volume tracking algorithm to capture the drop free surface. Later, Bussmann et al. [34], built on this model and simulated the splashing and fingering of a drop impact on a solid substrate. Pasandideh-Fard et al. [35] extended Bussmann's model to include for heat transfer and solidification in the case of molten metal droplets.

Gunjal et al. [36] used volume of fluid (VOF) based numerical model to study the dynamics of a drop impact. For different surface wettabilities, their simulation was able to successfully predict the spreading, splashing and other key features of the interaction. Accordingly, Lunkad et al. [37] used VOF approach and studied the spreading of drops on inclined surfaces. They investigated the effects of surface inclination, liquid properties and impact velocity on drop spreading. By considering static contact angle (SCA) and dynamic contact angle (DCA) models, they additionally studied the influence of surface wetting characteristics.

In contrary to these simulations for drops impact, less attention has been given to numerical studies of free liquid jets impinging on both stationary and moving surfaces. Many of the works available in literature considered submerged liquid jets to avoid the problem of capturing free surface. However, there have been few attempts to simulate the free surface liquid jets. Gradeck et al. [23] fundamentally studied the flow fields of a single water jet impinging on a moving plate for various jets and nozzle diameters, 17 mm and 20 mm. They numerically and experimentally identified the location and depth of the hydraulic jump for conditions used in the rolled metal cooling process. More recently, Fujimoto et al. [24] examined the flow characteristics of a water jet impinging on a surface covered with water film. Their numerical simulations were in good agreement with experimental observations. Later, they extended the simulations to include for two circular water jets [38]. They reported the effects of jet velocity, nozzle to plate distance, and nozzle to nozzle distance on detailed flow fields.

Several researchers studied liquid jets impingement phenomenon for heat transfer purpose. Tong [39] numerically examined the convective heat transfer of liquid jets impingement. They investigated several key parameters and found that jet velocity has significant influences on hydrodynamic development and heat transfer efficiency. Cho et al. [40] carried out three-dimensional numerical study to quantify the liquid surface depth and location for multiple jets in runout table cooling (ROT) processes. For different flow rates, they reported the free surface shape and liquid velocities on moving substrate. However, most of the works mentioned above are either for low jet and surface velocities or, more importantly, aimed at heat transfer and cooling processes.

## 5.1 Numerical Method

In this section the numerical formulations employed to obtain the CFD results are presented. The governing equations are briefly explained. Then, they are followed by the computational domain and associated boundary conditions. Volume-of-fluid (VOF) CFD simulations are carried out to provide a full description of the flow field of a laminar Newtonian jet spreading over a smooth moving surface. The jet Reynolds number and Weber number of the simulations are respectively in the range of 50-1000 and 100-8000. The jet-to-surface velocity ratio is in the range of 0.2-1.5.

### 5.1.1 Governing Equations

The VOF-based numerical model is used to simulate the steady liquid jet impingement. VOF approach solves the conservation of mass and momentum equations for the mixture phase augmented with a continuity equation for the volume fraction of one of the phases to track the interface. The volume fraction for the secondary phase obtained via the constraint  $\alpha_1 + \alpha_2 = 1$ . Given the flow is incompressible and the phases are Newtonian, the VOF model takes the following form

$$\frac{\partial \rho}{\partial t} + \vec{\nabla} \cdot (\rho \vec{V}) = 0 \quad (5-1)$$

$$\frac{\partial}{\partial t}(\rho \vec{V}) + \vec{\nabla} \cdot (\rho \vec{V} \vec{V}) = -\vec{\nabla} p + \vec{\nabla} \cdot \bar{\tau} + \rho \vec{g} + \vec{F}_{st} \quad (5-2)$$

$$\frac{\partial}{\partial t}(\alpha_1) + \vec{\nabla} \cdot (\alpha_1 \vec{V}) = 0 \quad (5-3)$$

Here  $\alpha_1$  is the volume fraction of the primary phase,  $\rho$  and  $\vec{V}$  are, respectively, the mixture density and the mixture velocity

$$\rho = \alpha_1 \rho_1 + \alpha_2 \rho_2 \quad (5-4)$$

$$\rho \vec{V} = \alpha_1 \rho_1 \vec{V}_1 + \alpha_2 \rho_2 \vec{V}_2 \quad (5-5)$$

With  $\rho_1$  and  $\rho_2$  being the density of the phases, and  $\vec{V}_1$  and  $\vec{V}_2$  being the velocity of the phases. The mixture stress tensor is given by

$$\bar{\tau} = \mu \left[ \vec{\nabla} \vec{V} + (\vec{\nabla} \vec{V})^T \right] \quad (5-6)$$

with  $\mu = \alpha_1 \mu_1 + \alpha_2 \mu_2$  the mixture viscosity;  $\mu_1$  and  $\mu_2$  are the viscosity of the phases.  $F_{ST}$  is the surface tension force incorporated into the momentum equation as a source term via the continuum surface force model proposed by Brackbill et al. [22]

$$\vec{F}_{ST} = (\sigma \kappa \hat{n} + \vec{\nabla}_s \sigma) \delta \quad (5-7)$$

where  $\sigma$  is the surface tension coefficient,  $\kappa$  is the mean curvature of the interface,  $\vec{\nabla}_s$  is the surface tension gradient along the phase interface surface,  $\hat{n}$  is the normal to the surface, and  $\delta$  denotes the interfacial Dirac distribution.

### 5.1.2 Dimensionless Governing Equations

Introducing  $T$  as the characteristic time scale,  $D$  the characteristic length scale (jet diameter),  $U$  the characteristic velocity scale (jet velocity or surface velocity), and  $P_0$  as the reference pressure, we obtain the following nondimensional variables

$$t^* = \frac{t}{T}, \quad \vec{x}^* = \frac{\vec{x}}{D}, \quad \vec{V}^* = \frac{\vec{V}}{U}, \quad p^* = \frac{p}{P_0}, \quad \vec{g}^* = \frac{\vec{g}}{g} \quad (5-8)$$

The mixture momentum equation renders dimensionless as follows

$$[St] \frac{\partial \vec{V}^*}{\partial t^*} + \vec{\nabla}^* \cdot (\vec{V}^* \vec{V}^*) = -[Eu] \vec{\nabla}^* p^* + \left[ \frac{1}{Re} \right] \vec{\nabla}^* \cdot \bar{\tau}^* + \left[ \frac{1}{Fr^2} \right] \vec{g}^* + \left[ \frac{1}{We} \right] \vec{F}_{ST}^* \quad (5-9)$$

which contains the following non-dimensional groups

$$St = \frac{D}{TU}, Eu = \frac{P_0}{\rho U^2}, Re = \frac{\rho UD}{\mu}, Fr = \frac{U}{\sqrt{gD}}, We = \frac{\rho U^2 D}{\sigma} \quad (5 - 10)$$

which are respectively, the Strouhal number, the Euler number, the Reynolds number, the Froude number, and the Weber number. It should be noted that in the above non-dimensionalization, we have used only one length scale  $D$  and one velocity scale  $U$ . A more rigorous approach should take the lamella thickness for non-dimensionalizing the coordinate axis perpendicular to the surface ( $z$ -coordinate) and the jet diameter for the coordinates in the plane of the surface ( $x$ - and  $y$ -coordinates).

### 5.1.3 Meshing and Boundary Conditions

Figure 5-1 shows the generic computational domain used for the simulations with the associated boundary conditions. The domain extends from 20D upstream to 80D downstream of the impingement point, where  $D$  is the jet diameter. The domain dimensions are given in Figure 5-1(a). The lateral walls, considered as the pressure outlet boundary condition, are extended to 40D to assure their impact on the jet flow is minimal. The typical computational mesh used in the simulations highlights the small mesh size used in regions of high velocity gradients and around the free surface.

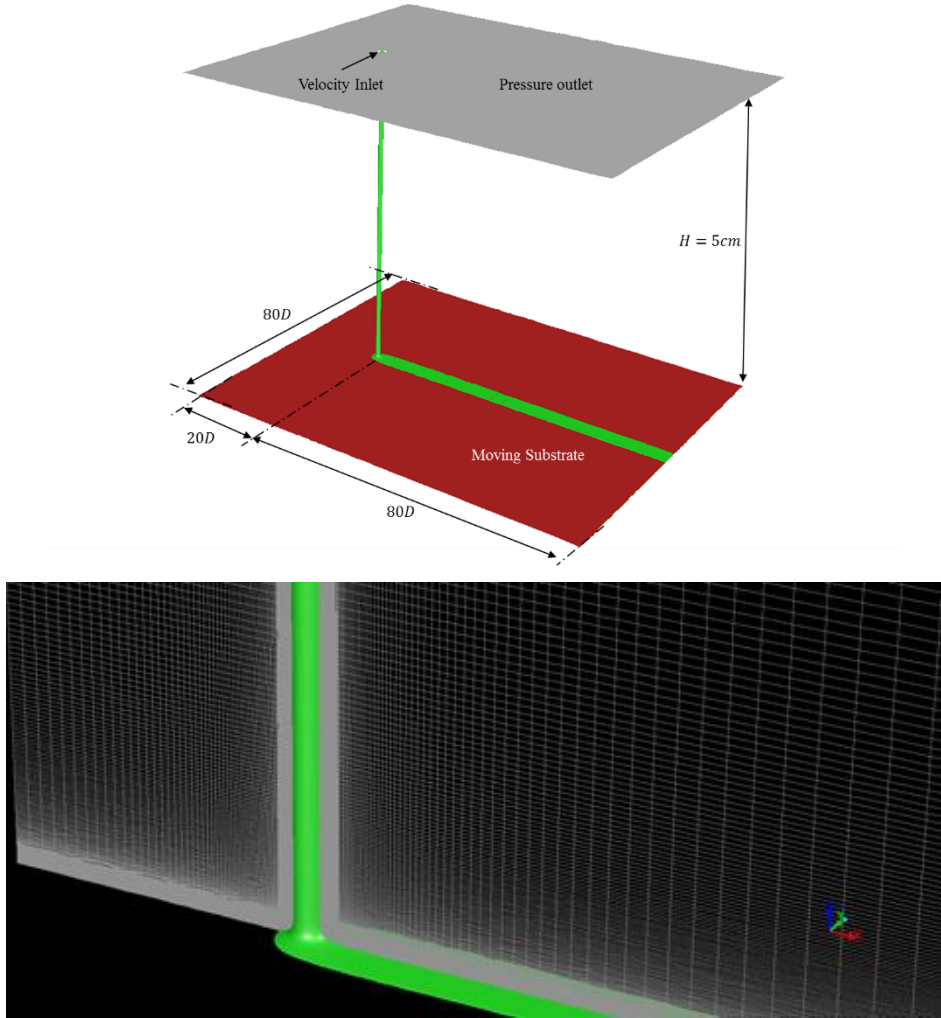


Figure 5-1 Schematic of the computational domain used for the simulations with the associated boundary conditions (Top); the lateral walls are also considered as the pressure outlet boundary condition. The typical computational mesh used in the simulation (bottom)

#### 5.1.4 Mesh Independency Check

To ensure that the obtained data are mesh-independent, several flows were simulated with different mesh densities. We refined the boundary layer mesh over the moving surface and structured mesh around the jet free surface. Additionally, we slightly refined the mesh in the outer region of the flow. Figure 5-2 presents the free surface profile around the impingement point on the symmetry plane for the typical coarse and intermediate meshes. The conditions are given in the caption. In general, the lamella thickness (on the order of 50-100 microns) is captured by 3

computational cells on the coarse mesh, 6 cells on intermediate mesh, and 10 cells on the fine mesh. The velocity profiles within the lamella thickness on the symmetry plane at  $x=1.1D$  downstream and upstream of the impingement point for different mesh intensities are shown in Figure 5-3. To estimate the discretization error, we followed the procedure recommended in [41] for the velocity profiles and lamella thicknesses errors. The numerical uncertainty in the fine-grid solution was found to be 7.2% for lamella thicknesses and at most 9.4% for the velocity profiles.

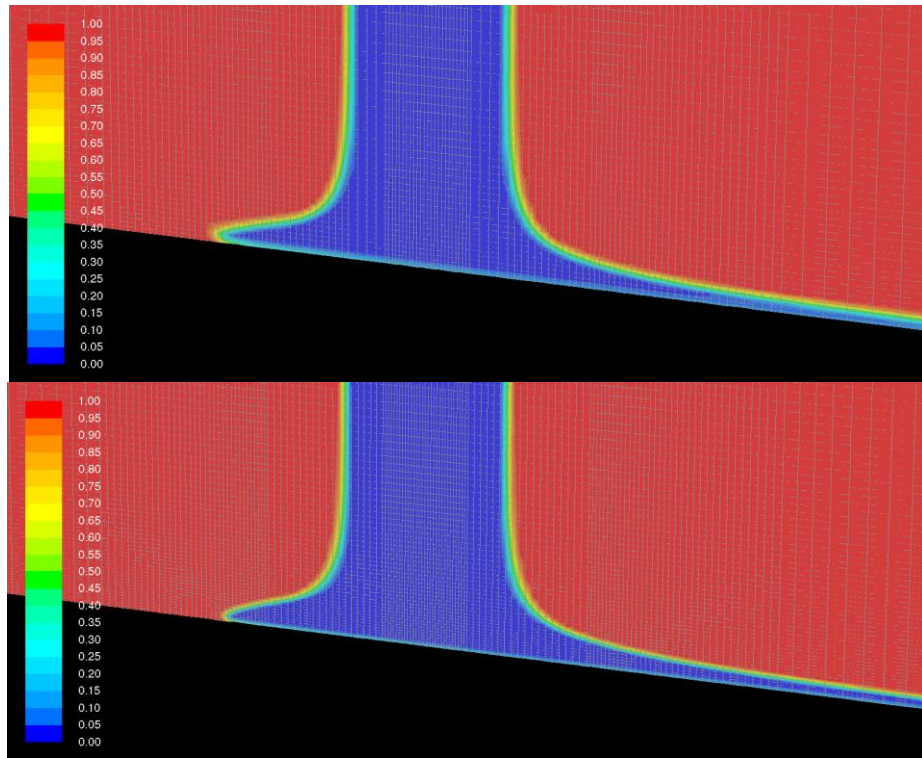


Figure 5-2 Free surface profile around the impingement point for the typical coarse mesh (top) and intermediate mesh (bottom). Red color indicates the region filled with air and the blue color indicates liquid. For this particular test, the substrate velocity was  $60 \text{ ms}^{-1}$ , the jet velocity was  $15 \text{ ms}^{-1}$ , the jet diameter was  $650 \mu\text{m}$ , and the liquid viscosity, density, and surface tension were respectively  $40 \text{ mPa.s}$ ,  $1100 \text{ kg.m}^{-3}$ , and  $0.065 \text{ N.m}^{-1}$ . The corresponding jet Reynolds number and Weber number are 268 and 2475.

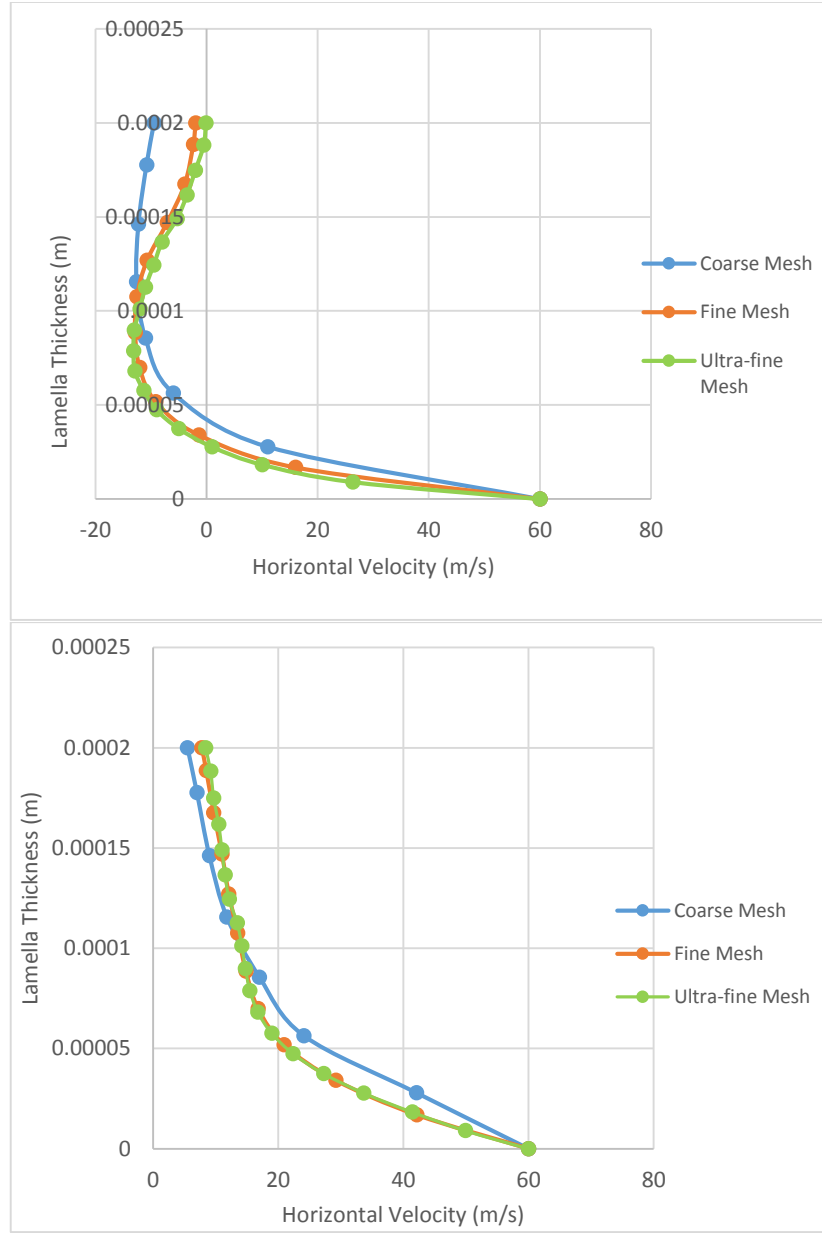


Figure 5-3 Velocity profile within the lamella thickness for different mesh intensities. The conditions are given in the caption of Figure 3. The profile is extracted along a line normal to the substrate at  $x=1.1D$  upstream of the impingement point (top) and downstream of the impingement point (bottom).

### 5.1.5 Validation With Experiment

The numerical results are validated with data measured on the spinning disk experimental apparatus. Recently, Guo [27] studied the effects of various parameters such as jet and surface

speeds, and orifice diameter on lamella geometry. He also made detailed measurements of the dimensions of the liquid surface. Figure 5-4 shows the top view of jet impingement and the lamella dimensions.

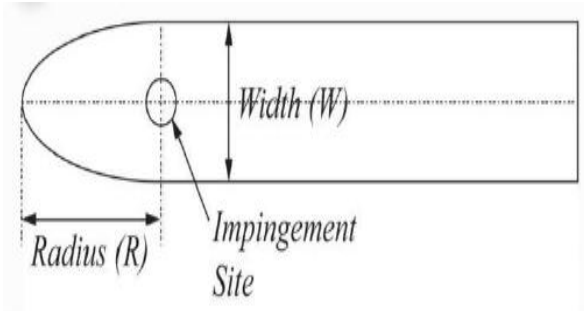


Figure 5-4 Lamella dimensions (top view of jet impingement)

The lamella width and radius from CFD simulations are compared with experimental results in Figure 5-5. The free surface of the liquid was defined to be the location in the flow where volume fraction is 50%. An interesting result is that the ratio  $W/R$  is almost constant, independent of the liquid' properties, the jet and substrate speeds, and the jet diameter, as first reported by Guo [27]. The numerical predictions are generally in very good agreement with experimental findings (5.8% rms variance), and almost lie within the error bands.

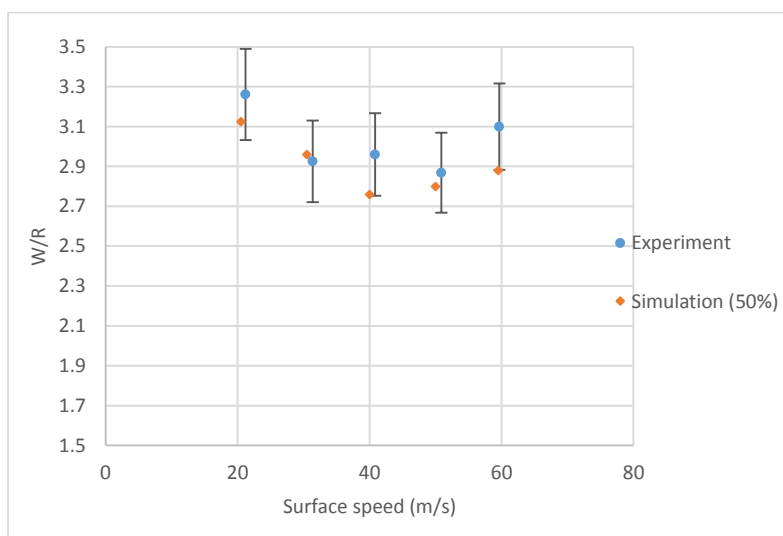


Figure 5-5  $W/R$  versus surface speed for constant jet velocity of  $12\text{ ms}^{-1}$  and viscosity of  $65.3\text{ mPa.s}$

## 5.2 Results and Discussions

The path-line of liquid jet is obtained from simulation (Figure 5-6). The simulation parameters are given in the capture of figure.

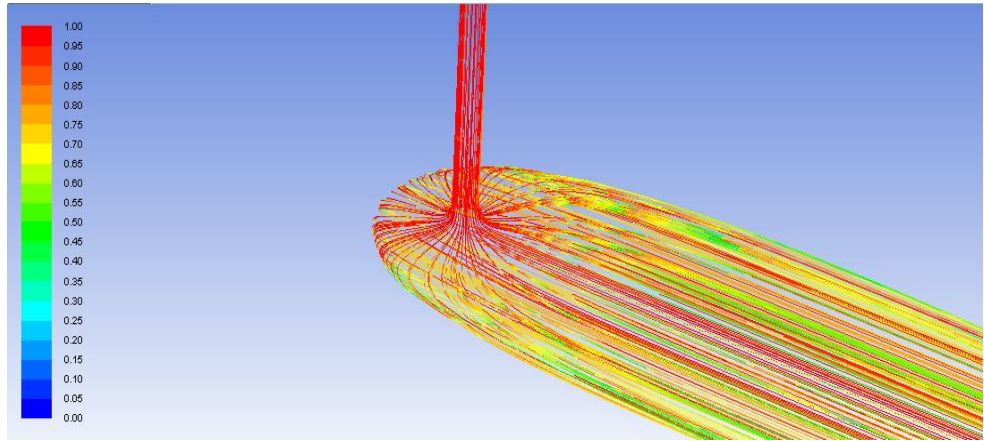
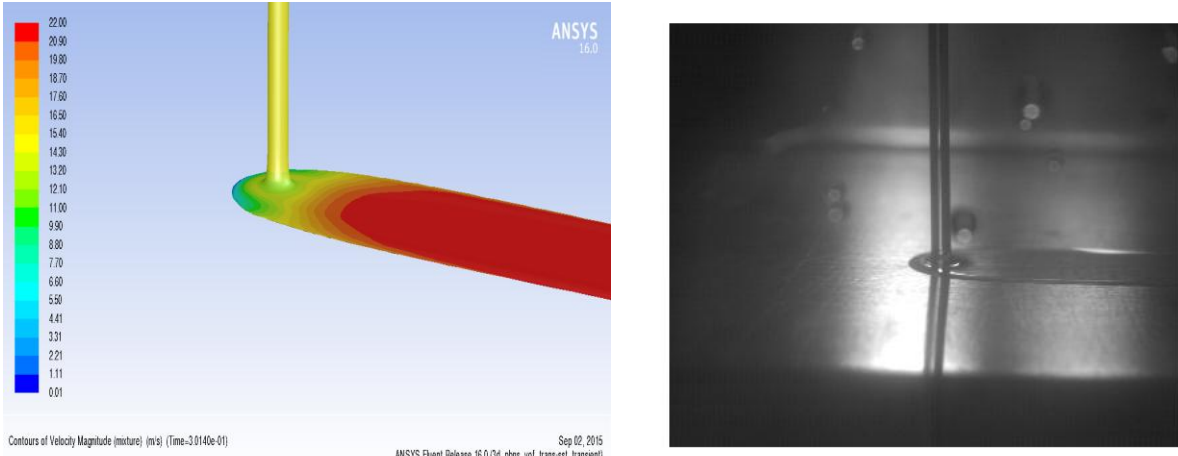
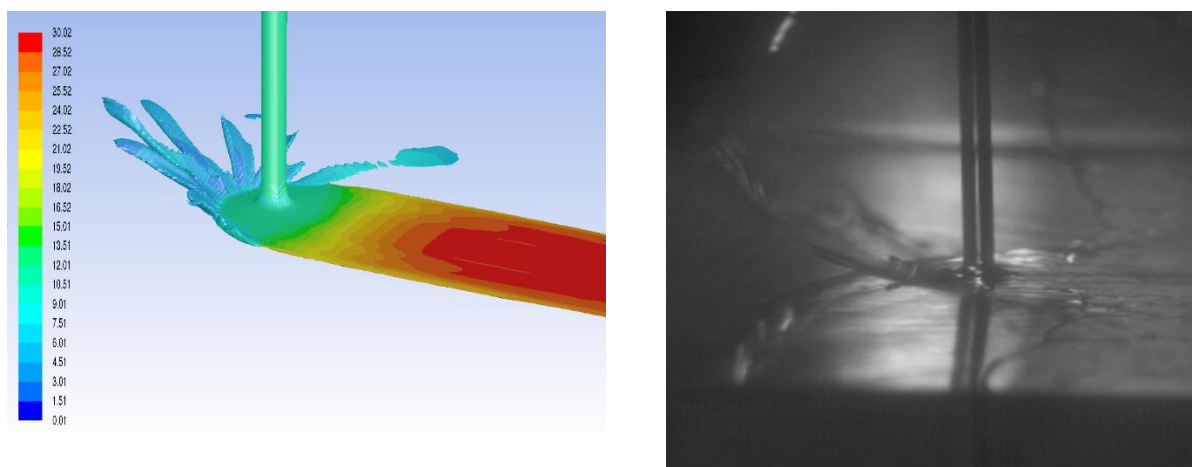


Figure 5-6 Path-line of liquid jet impinging on a moving surface. For this particular test, the substrate velocity was  $22 \text{ ms}^{-1}$ , the jet velocity was  $15 \text{ ms}^{-1}$ , the jet diameter was  $1300 \mu\text{m}$ , and the liquid viscosity, density, and surface tension were respectively  $40 \text{ mPa.s}$ ,  $1100 \text{ kg.m}^{-3}$ , and  $0.065 \text{ N.m}^{-1}$

Figure 5-7 shows the splashing-spreading pattern for both experiments and simulations. Although numerical simulations successfully predict the outcome of jet impact for these two conditions, the splash threshold obtained via simulation is not in good agreement with experiments. First reason is static contact angle (SCA) model was used in the CFD simulation; however, it has been proven that dynamic contact angle (DCA) is more successful in capturing the splash threshold [37]. More importantly, surface roughness is not included in the simulation. Several works have shown the significant influences of surface rough on the splash/nonsplash boundary.



$$a) D = 1300 \mu\text{m}, \mu = 0.065 \text{ Pa.s}, \rho = 1150 \frac{\text{kg}}{\text{m}^3}, \sigma = 0.065 \frac{\text{N}}{\text{m}}, V_{jet} = 15 \frac{\text{m}}{\text{s}}, V_{surface} = 22 \frac{\text{m}}{\text{s}}$$



$$b) D = 1300 \mu\text{m}, \mu = 0.014 \text{ Pa.s}, \rho = 1150 \frac{\text{kg}}{\text{m}^3}, \sigma = 0.065 \frac{\text{N}}{\text{m}}, V_{jet} = 15 \frac{\text{m}}{\text{s}}, V_{surface} = 30 \frac{\text{m}}{\text{s}}$$

Figure 5-7 Outcome of jet impact for simulation and experiment, a) Deposition, b) Splash

Figure 5-8 highlights the lamella dimensions in comparison with experiment measurements. The lamella dimensions are plotted as a function of surface speeds for constant jet velocity. The free surface of the liquid was defined to be the location in the flow where volume fraction is 50% and 90%. It can be observed that volume of fraction of 50% is in more agreement with experiments. However, the agreement between experiments and simulations is less good if

one considers separately the values of W and R rather than the ratio of the two (Figure 5-5); both W and R are slightly over predicted (12.1% on average) by CFD simulations.

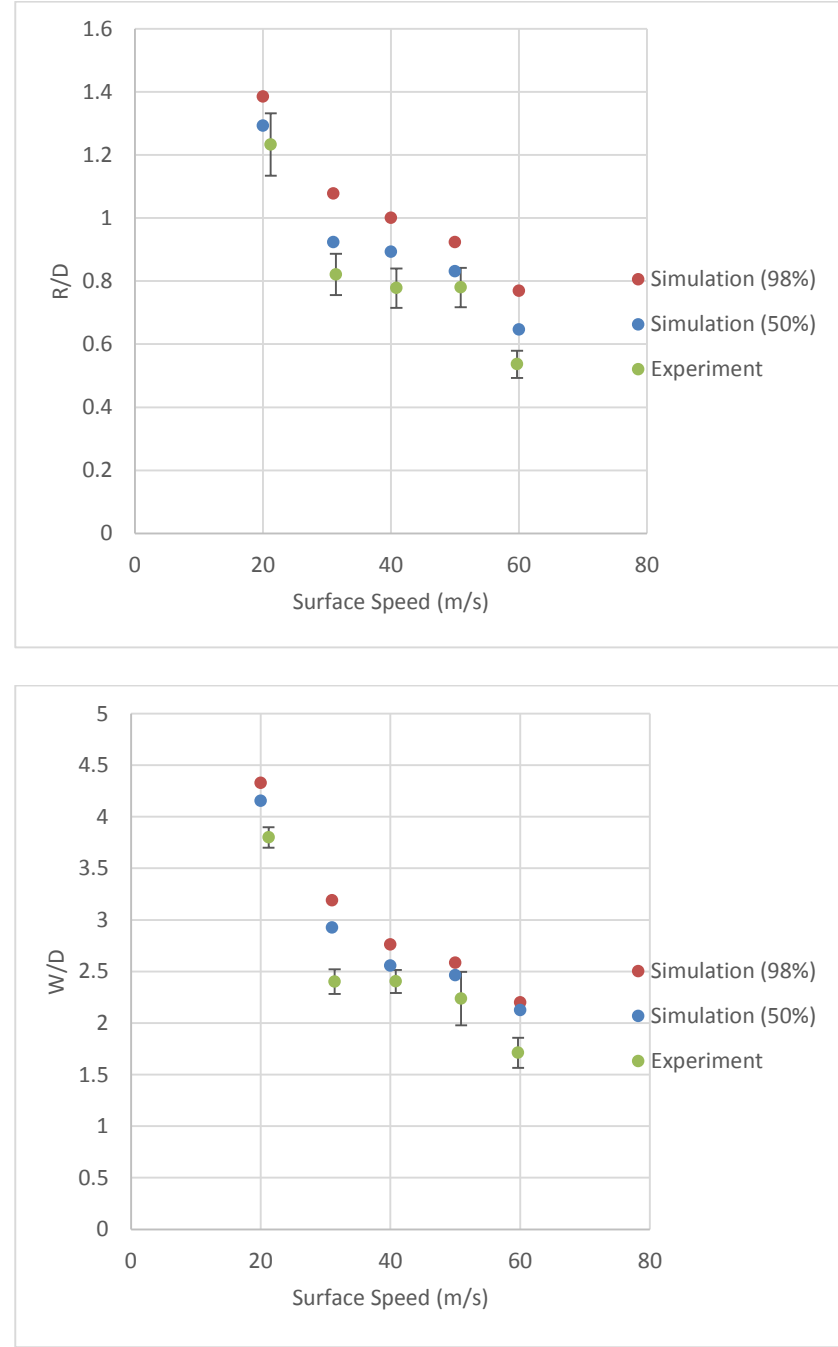


Figure 5-8 R/D and W/D versus surface speed at constant jet velocity of  $12 \text{ m.s}^{-1}$

Finally, some graphs can be obtained from simulation which are not feasible via experiment. Figure 5-9 displays the velocity profiles for different jet flow rates. The surface speed is constant, 30 m/s, and the velocities are plotted downstream of impingement point. Due to no slip boundary conditions, the velocity is 30 m/s at  $z=0$ . Assuming that the lamella thickness is around 0.00012 m, the velocity does not go to zero sharply and this is the nature of VOF-based numerical simulation.

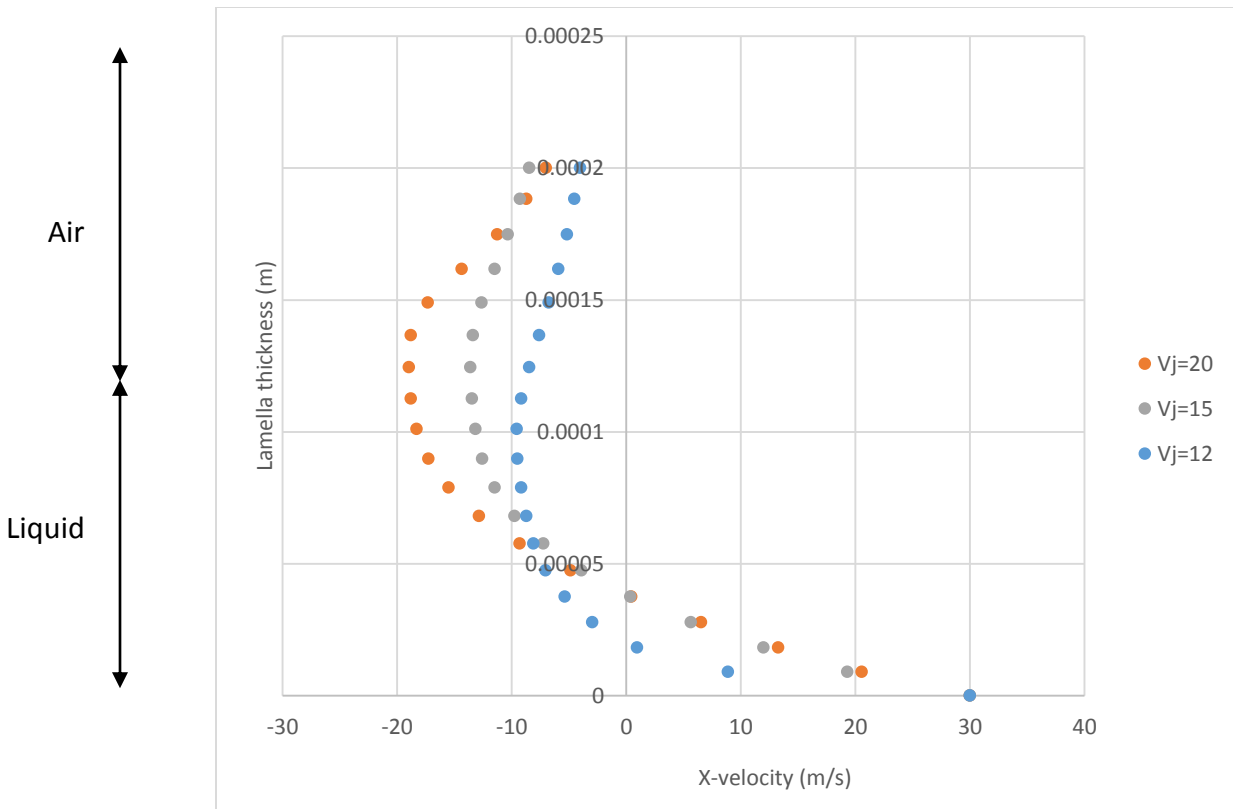


Figure 5-9 Horizontal velocity profiles within lamella

## **Chapter 6 : Conclusions and Recommendations**

### **6.1 Conclusions for Liquid Friction Modifier (ALLEVIATE®)**

ALLEViate® is a liquid friction modifier that Kelsan Technological Corporation applies to slippery rails. ALLEViate® contains large sand particles to improve rail-wheel traction. The particle size distribution was measured. The nozzle diameter was chosen at least five times greater than the mean particle sizes (0.2-0.4 mm) to avoid the nozzle clogging. Rheological data showed that ALLEViate® is a non-Newtonian fluid with shear thinning and viscoplastic properties. The value of yield stress was found to be 7.4 Pa.

An experimental study was carried out to investigate a steady ALLEViate® jet impingement on a moving surface. High-speed imaging was used to visualize the impingement phenomenon. The influences of viscosity and particle presence were studied. For different viscosities, results were consistent with previous findings by Guo [27] and Keshavarz et al. [19] for liquid jets, indicating that the jet is more prone to splash for lower viscosities. It was observed that the particle addition has little impacts on the splash threshold and ALLEViate®'s low transfer efficiency is mainly caused by the base fluid.

The desired flow rate is 3 Lit/min. Based on Figure 3-5, 3 Lit/min flow rate requires jet velocity of 4.1 m/s with 2.1 mm orifice diameter. Figure 3-7 demonstrates that for the jet velocity of 4.1 m/s, deposition occurs for surface speeds lower than 18 m/s. Thus, higher surface speeds lead to splash and waste of materials. Finally, Figure 3-11 suggests that the cross wind, even with speed of 19.9 m/s, cannot deflect the jet excessively.

## **6.2 Conclusions for Newtonian Suspension Jets Impingement on Moving Surface**

An experimental study was performed to study the interaction of Newtonian particle-laden jets on a high speed dry moving surface. The effects of particle size, volume fraction, surface roughness, jet and surface velocities were examined. Five different water-glycerin solutions with various volume fractions were used to isolate the influence of viscosity. The particle density was matched to the fluid density to yield neutrally buoyant suspension. Again, high speed imaging was employed to visualize the interaction and lamella geometry. The key findings of this study are:

- The suspensions show Newtonian viscosity for low concentrations studied, typically up to 10 %. But, it should be noted that particles increase the viscosity.
- The trend of splash threshold for particle-laden jets is generally in good agreement with previous findings for pure liquid jets. For the ranges studied, higher jet and surface velocities, lower viscosity, and higher surface roughness height all make jets more prone to splash.
- Interestingly, it was observed that addition of hollow glass spheres to Newtonian jets enhances deposition and postpones splash. Although the liquid jet consisting the glass beads were completely stable, the wave-form instability was observed downstream of the lamella. However, lamella dimensions and shape remained unchanged.
- In contrast, jets with larger particles in suspension are more prone to splash than single phase jets of the same viscosity. It is speculated that the non-monotonic dependence of the splash threshold on the particle size occurs when the particle diameter is comparable to lamella thickness.

### **6.3 Conclusions for Numerical Simulation of Laminar Liquid Jet Impingement**

Three-dimensional numerical study was carried out to simulate the steady laminar jet impingement on a moving surface. VOF approach was employed to track the free surface of the flow. Static contact angle (SCA) was used to simulate the interaction. Simulations were validated with experiments on spinning disk apparatus. Simulations successfully predict the spreading of a liquid jet. Lamella dimensions obtained via simulation are generally in good agreement with experimental results (5.8% rms variance). The agreement between experiments and simulations is less good if one considers separately the values of W and R rather than the ratio of the two. Both W and R are slightly over predicted and h (lamella thickness) is slightly under predicted. However, the simulations could not identify the splash threshold because it did not include for surface roughness and dynamic contact angle.

### **6.4 Recommendations for Future Work**

To further understand how particle-laden jets interact with a high-speed moving surface, following areas should be further investigated:

- More detailed studies of influences of mean particle sizes and volume fractions on splash-nonsplash boundaries.
- Understanding how particles in neutrally buoyant suspensions behave before and after impact to explain why particle size plays an essential role in determining the splash threshold.

- Adding solid particles to non-Newtonian jets, particularly viscoplastic fluids, and accordingly finding the splash thresholds and lamella dimensions.

Numerical study can be extended to simulate non-Newtonian fluids and suspensions. Simulation of suspension jets may shed light to experimental observations. Additionally, simulation can be extended to include dynamic contact angle (DCA) and surface roughness. Through including the surface roughness and DCA, numerical results will be able to successfully predict the splash threshold.

## Bibliography

- [1] Cotter, J., Eadie, D.T., Elvidge, D., Hooper, N., Robert, J., Makowsky, T., and Liu, Y., 2005, Top of Rail Friction Control: Reductions in Fuel and Greenhouse Gas Emissions. In: Proc. Of the 2005 Conference of the International Heavy Haul Association (Rio de Janeiro), pp. 327-334.
- [2] Y. Suda, T., Iwasa, H., Komine, T., Fuji, K., Matsumoto, N., Ubukata, T., Nakai, M.Tanimoto, Y. Kishimoto, 2003, The basic study on friction control between wheel and rail (experiments by test machine and scale model vehicle), in: Proceedings of the 6th International Conference on Contact Mechanics and Wear of Rail/Wheel Systems (CM2003), Gothenburg, Sweden. vol. II, pp. 343–348.
- [3] Eadie, D.T., Bovey, E., and Kalousek, J., 2002, The role of friction control in effective management of the wheel/rail interface, Railway Technical Conference, pp. 432-481.
- [4] Miva, M., & Mizuno, M. (2014). Modeling an Optimal Track Maintenance Schedule in Consideration of Train Derailment Risk. Quarterly Report of RTRI, 55(1), 51-59.
- [5] Rein, M., 1993, Phenomena of Liquid Drop Impact on Solid and Liquid Surfaces, Fluid Dynamics Research, 12:61-93.
- [6] Yarin, A.L., 2006, Drop Impact Dynamics: Splashing, Spreading, Receding, Bouncing, Annual Review of Fluid Mechanics, 38:159-192.
- [7] Rioboo R, Marengo M, Tropea C., 2003, Time evolution of liquid drop impact onto solid, dry surfaces. Exp Fluid. 2002;33:112–124.
- [8] Range, K., and Feuillebois, F., 1998, Influence of Surface Roughness on Liquid Drop Impact, Journal of Colloid and Interface Science, 203:16-30.
- [9] Mundo, C., Sommerfield, M., and Tropea, C., 1995, Droplet-Wall Collisions: Experimental Studies of the Deformation and Breakup Process, International Journal of Multiphase Flow, 21:151-173.

- [10] Chen, R.H., Wang, H.W., 2005. Effects of tangential speed on low–normal-speed liquid drop impact on a non-wettable solid surface. *Exp. Fluid* 39, 754– 760.
- [11] Povarov, O.A., Nazarov, O.I., Ignat'evskaya, L.A., and Nikol'Skii, A.I., 1976, Interaction of drops with boundary layer on rotating surface, *Journal of Engineering Physics*, 31:1453-1456.
- [12] Courbin, L., Bird, J.C., and Stone, H.A., 2006, Splash and anti-Splash: Observation and Design. *Chaos*, 16:041102.
- [13] Bird, J. C., Tsai, S.S.H., and Stone, H.A., 2009, Inclined to Splash: Triggering and Inhibiting a Splash with Tangential Velocity, *New Journal of Physics*, 11:1-6(2009).
- [14] Luu, H.L., Forterre, Y., 2009, Drop impact of yield-stress fluids, *J. Fluid Mech.* 632, 301.
- [15] Nicolas, M., 2005, Spreading of a drop of neutrally buoyant suspension, *J. Fluid Mech.* 545, 271.
- [16] Cossali, G.E., Coghe, A., Marengo, M., 1997, The impact of a single drop on a wetted solid surface, *Exp. in Fluids*, 463-472.
- [17] Peters, I.R., Xu, Q., M. Jaeger, H., 2013, Splashing Onset in Dense Suspension Droplets. *Physical Review Letter* 111, 028301.
- [18] Grishaev, V., 2015, Impact of particle-laden drops on substrates with various wettability, PhD Dissertation, École Polytechnique De Bruxelles.
- [19] Keshavarz, B., Green, S. I., Davy, M. H., & Eadie, D. T., 2011, Newtonian liquid jet impaction on a high-speed moving surface. *International Journal of Heat and Fluid Flow*, 32(6), 1216-1225.
- [20] Watson, E. J., 1964. The radial spread of a liquid jet over a horizontal plane. *Journal of Fluid Mechanics*, 20(03), 481-499.
- [21] Nakoryakov, V. E., Pokusaev, B. G., Troyan, E. N., 1978, Impingement of an Axisymmetric Liquid Jet on a Barrier. *Int. J. Heat Mass Transfer* 21, 1175-1184

- [22] Zumbrunnen, D.A., 1991, Convective heat and mass transfer in the stagnation region of a laminar planar jet impinging on a moving surface, *Journal of Heat Transfer*, 113:3 563 570.
- [23] Gradeck, M., Kouachi, A., Dani, A., Arnoult, D., Borean, J., 2006, Experimental and numerical study of the hydraulic jump of an impinging jet on a moving surface. *Experimental thermal and fluid science*, 30(3), 193-201.
- [24] Fujimoto, H., Suzuki, Y., Hama, T., Takuda, H., 2011, Flow Characteristics of Circular Liquid Jet Impinging on a Moving Surface Covered with a Water Film. *ISIJ international*, 51, 1497-1505.
- [25] Kumar, P., 2011, Liquid Jet Interaction with a Moving Surface, M.A.Sc. Thesis, UBC.
- [26] Moulson, J. B. T., & Green, S. I., 2013, Effect of ambient air on liquid jet impingement on a moving substrate. *Physics of Fluids*, 25(10), 102106.
- [27] Guo, Y., 2014, Newtonian and viscoelastic liquid jet impingement on a moving surface, M.A.Sc. Thesis, UBC.
- [28] Shirazi, A. S., 2015, Transient Jet Impaction On A High Speed Moving Surface, M.A.Sc. Thesis, UBC.
- [29] Yamamura, M., Matsunaga, A., Mawatari, Y., Adachi, K., Kage, H., 2006, Particle-assisted dynamic wetting in a suspension liquid jet impinged onto a moving solid at different flowrates. *Chemical Engineering Science*, 61 5421 –5426
- [30] Dressler, D.M., 2006, An experimental investigation of Newtonian and non-Newtonian spray interaction with a moving surface, M.A.Sc. Thesis, UBC.
- [31] Mangesana, N., Chikuku, R.S., Mainza, A.N., Govender, I., 2008, The effect of particle sizes and solids concentration on the rheology of silica sand based suspensions. *The Journal of Southern African Institute of Mining and Metallurgy*, 57-64.
- [32] Tsai, S.C., Botts, D., Plouff. J., 1992, Effects of particle properties on the rheology of concentrated noncolloidal suspensions. *Journal of Rheology* 36, 1291.
- [33] Bussmann, M., Mostaghimi, J., Chandra, S., 1999, On a three-dimensional volume tracking model of droplet impact. *Physics of Fluids*, 11, 1406.

- [34] Bussmann, M., Chandra, S., M., Mostaghimi, J., 2000. Modeling the splash of a droplet impacting a solid surface. *Physics of fluids*, 12, 3121.
- [35] Pasandideh-Fard, M., Chandra, S., Mostaghimi, J., 2002. A three-dimensional model of droplet impact and solidification, *International Journal of Heat and Mass Transfer*, 22–29.
- [36] Gunjal, P.R., Ranande, V.V., Chaudhari, V., 2005, Dynamics of Drop Impact on Solid Surface: Experiments and VOF Simulations. *AICHE Journal*, 51: 59–78.
- [37] Lunkad, S.F., Buwa, V.V., Nigam, K.D.P., 2007, Numerical simulations of drop impact and spreading on horizontal and inclined surfaces. *Chemical Engineering Science*, 7214 – 7224.
- [38] Fujimoto, H., Lee, Y., Kato, R., Hama, T., Takuda, H., 2013, Experimental and Numerical Study of Twin Circular Water Jets Impinging on a Moving Thin Film. *ISIJ International*, No. 8, pp. 1427–1435.
- [39] Tong, A.Y., 2011, A Numerical Study On The Hydrodynamics And Heat Transfer Of A Circular Liquid Jet Impinging Onto A Substrate, *Numerical Heat Transfer*, 44:1, 1-19.
- [40] Cho, M.J., Thomas, B.G., Lee, P.J., 2008, Three-Dimensional Numerical Study of Impinging Water Jets in Runout Table Cooling Processes. *The Minerals, Metals & Materials Society and ASM International*, s11663-008-9160-8.
- [41] Roache, P.J., 1997, Quantification of uncertainty in computational fluid dynamics, *Annual Review of Fluid Mechanics*, 29; pp. 123-160.